PHYSICAL REVIEW D **86,** 024026 (2012)

Correlated gravitational wave and neutrino signals from general-relativistic rapidly rotating iron core collapse

C. D. Ott,[1,2,3,*] E. Abdikamalov,[1] E. O'Connor,[1] C. Reisswig,[1] R. Haas,[1] P. Kalmus,[4,1] S. Drasco,[5,1] A. Burrows,[6] and E. Schnetter[7,8,3]

[1]*TAPIR, MC 350-17, California Institute of Technology, 1200 E California Boulevard, Pasadena, California 91125, USA*
[2]*Kavli Institute for the Physics and Mathematics of the Universe, The University of Tokyo, Kashiwa, Japan 277-8583*
[3]*Center for Computation & Technology, Louisiana State University, 216 Johnston Hall, Baton Rouge, Louisiana 70803, USA*
[4]*LIGO Laboratory, MC 100-36, California Institute of Technology, 1200 E California Boulevard, Pasadena, California 91125, USA*
[5]*California Polytechnic State University, 1 Grand Avenue, San Luis Obispo, California 93407, USA*
[6]*Department of Astrophysical Sciences, 4 Ivy Lane, Princeton, New Jersey, 08544, USA*
[7]*Perimeter Institute for Theoretical Physics, 31 Caroline Street N., Waterloo, Ontario N2L 2Y5, Canada*
[8]*Department of Physics, University of Guelph, 50 Stone Road East, Guelph, Ontario N1G 2W1, Canada*

(Received 21 April 2012; revised manuscript received 20 June 2012; published 13 July 2012)

We present results from a new set of three-dimensional general-relativistic hydrodynamic simulations of rotating iron core collapse. We assume octant symmetry and focus on axisymmetric collapse, bounce, the early postbounce evolution, and the associated gravitational wave (GW) and neutrino signals. We employ a finite-temperature nuclear equation of state, parametrized electron capture in the collapse phase, and a multispecies neutrino leakage scheme after bounce. The latter captures the important effects of deleptonization, neutrino cooling and heating and enables approximate predictions for the neutrino luminosities in the early evolution after core bounce. We consider $12-M_\odot$ and $40-M_\odot$ presupernova models and systematically study the effects of (i) rotation, (ii) progenitor structure, and (iii) postbounce neutrino leakage on dynamics, GW, and neutrino signals. We demonstrate that the GW signal of rapidly rotating core collapse is practically independent of progenitor mass and precollapse structure. Moreover, we show that the effects of neutrino leakage on the GW signal are strong only in nonrotating or slowly rotating models in which GW emission is not dominated by inner core dynamics. In rapidly rotating cores, core bounce of the centrifugally deformed inner core excites the fundamental quadrupole pulsation mode of the nascent protoneutron star. The ensuing global oscillations ($f \sim 700$–800 Hz) lead to pronounced oscillations in the GW signal and correlated strong variations in the rising luminosities of antineutrino and heavy-lepton neutrinos. We find these features in cores that collapse to protoneutron stars with spin periods $\lesssim 2.5$ ms and rotational energies sufficient to drive hyperenergetic core-collapse supernova explosions. Hence, GW or neutrino observations of a core-collapse event could deliver strong evidence for or against rapid core rotation. Joint GW + neutrino observations would allow one to make statements with high confidence. Our estimates suggest that the GW signal should be detectable throughout the Milky Way by advanced laser-interferometer GW observatories, but a water-Cherenkov neutrino detector would have to be of near-megaton size to observe the variations in the early neutrino luminosities from a core collapse event at 1 kpc.

DOI: 10.1103/PhysRevD.86.024026 PACS numbers: 04.25.D−, 04.30.Db, 04.30.Tv, 97.60.Bw

I. INTRODUCTION

The collapse of massive stars ($8M_\odot \lesssim M \lesssim 130M_\odot$ at zero-age main-sequence [ZAMS]) proceeds in a generic way: the electron-degenerate core separates into a homologously collapsing *inner core* and a supersonically collapsing outer core. At densities near nuclear, the nuclear equation of state (EOS) stiffens, leading to core bounce and the sudden reversal of the inner core's infall velocity, imparting kinetic energy onto the supernova shock. The latter initially rapidly propagates outward into the still infalling and sonically disconnected outer core, but soon, weakened by the work afforded to the dissociation of heavy nuclei and by neutrino losses, succumbs to the outer core's ram pressure, stalls, and turns into an accretion shock. The shock must be revived to drive an explosion and produce a core-collapse supernova, leaving behind a neutron star; otherwise the protoneutron star (PNS) quickly, within ∼0.5–3 s, accumulates sufficient mass to collapse to a black hole [1,2].

The currently favored mechanism for shock revival (see, e.g., [1,3–6]) relies on a combination of neutrino energy deposition in the region behind the shock with multidimensional convective- and advective-acoustic instabilities. However, alternative mechanisms exist (e.g., [7,8]). In particular, massive stars with rapid rotation in their core may experience magnetorotational explosions in which magnetic fields, amplified by rapid rotation (e.g., via the

*cott@tapir.caltech.edu

 © 2012 American Physical Society

magnetorotational instability [9,10]), drive powerful bipolar explosions [11–14]. Most massive stars are expected to have slowly spinning cores [15,16], but of order 1% [17] may have sufficient core angular momentum for a magnetorotational explosion. This special group of rapidly spinning massive stars has also been proposed as progenitors of long gamma-ray bursts (GRBs) [17,18], since all currently discussed long-GRB models require rapid rotation in combination with a compact, hydrogen-poor stellar envelope to produce the characteristic Type Ib/c supernova features observed in GRB afterglows (e.g., [19]). Rapid rotation could also play a key role in very energetic non-GRB core-collapse supernovae (e.g., [20]) whose total energy output may be enhanced by magnetar spindown via dipole radiation [21,22] or by a magnetohydrodynamic (MHD) propeller ejecting fallback material [23].

Probing the role of rotation at the heart of core-collapse supernovae and long GRBs with electromagnetic waves is difficult, since they only provide an image of optically thin regions far away from the core. Much more direct information is carried by neutrinos and gravitational waves. Both are emitted inside the core where the deciding dynamics occur and travel to observers on Earth essentially unimpeded by intervening material. Neutrinos carry primarily thermodynamic and structural information about their source (e.g., [24–27]) while gravitational waves (GWs), owing to their quadrupole nature, provide complementing information on the multidimensional dynamics of the core (e.g., [24,28–31]). The combined observation of neutrinos and GWs from the next nearby core-collapse event may place stringent constraints on rotation in the core in particular and on core-collapse supernova physics in general (see, e.g., [24,32–34] and references therein). This, however, will require robust theoretical neutrino and GW signal predictions to be contrasted with observations.

Reliable modeling of the GW signal of rotating core collapse and bounce requires, in the ideal case, three-dimensional (3D) general relativity, microphysical EOS, progenitor data from stellar evolutionary calculations, energy-dependent multispecies neutrino transport, and MHD. Such complete models of stellar collapse still pose a formidable technical and computational challenge, but much progress in understanding the GW signature of core collapse and the subsequent core-collapse supernova evolution has been made in the past decade. We refer the reader to recent overview articles by Kotake [31] and Ott [28] for a comprehensive discussion of the range of potential GW emission processes in core-collapse supernovae and focus in the following only on GW emission from rotating core collapse, bounce, and the early postbounce evolution.

Pioneering axisymmetric (2D) work on the GW signal of rotating core collapse and bounce relied on Newtonian gravity with [35–38] or without [39,40] the inclusion of microphysical aspects such as a finite-temperature nuclear EOS and/or neutrino treatment. These studies identified three types of GW signal morphologies: *Type I* signals exhibit a prominent large negative spike associated with the tremendous deceleration and re-expansion of the inner core at bounce and a subsequent short ringdown feature emitted as the core settles into its new equilibrium. *Type II* show multiple pronounced peaks correlated with repeated large-scale postbounce contractions and re-expansions (''multiple bounces'') of extremely rapidly rotating inner cores that experience bounce due to the centrifugal force. *Type III* signals are associated with very small inner core mass, leading to a low-amplitude bounce spike with typically a positive peak value.

Early 2D general-relativistic (GR) models also used simplified microphysics [41,42], but more recent ones [43–45] employed microphysical EOS and deleptonization during collapse (but not after bounce). The latter set of studies showed that, due to a combination of deleptonization during collapse (which reduces the inner core mass) and general relativistic gravity, the GW signal of rotating core collapse has a generic morphology corresponding to the previously identified Type I signal shape. The multiple-bounce Type II dynamics and GW signals do not occur, while Type III signals may result from the accretion-induced collapse of rapidly rotating massive O-Ne white dwarfs [46]. These studies also demonstrated that the peak signal amplitude and characteristic GW frequency are determined primarily by the mass and angular momentum of the inner core at bounce. Waveform details are expected to depend on the nuclear EOS, progenitor core structure and thermodynamics, angular momentum distribution in the core, and deleptonization history during collapse [44,46,47].

MHD effects on the dynamics and GW signature of rotating collapse and bounce have been considered by [14,45,47–52]. While MHD can be crucial in driving an explosion in the postbounce phase, these studies showed that rotating collapse, bounce and the very early postbounce evolution (within $\lesssim$ 20–25 ms of bounce) and the associated GW signal are essentially unaffected by MHD effects unless the precollapse magnetization is set to extreme values $\gtrsim 10^{12}$ G. Even in extreme cases, current stellar evolutionary studies suggest $B \lesssim 10^{9}$ G [16,17].

3D core-collapse simulations were first attempted by Bonazzola and Marck [53], who studied only the collapse phase. The first set of studies investigating the GW signal of bounce and postbounce evolution in 3D started from 2D simulations of the collapse phase, relied on simplified microphysics and were carried out in Newtonian [54] or GR gravity [55]. They focused on extremely rapidly rotating configurations and found nonaxisymmetric dynamics developing in models with ratios of rotational kinetic energy to gravitational energy $T/|W| \gtrsim 27\%$ (see, e.g., [56] for a review of rotational instabilities). More recent 3D simulations that started at the onset of collapse and included microphysics and deleptonization before bounce

[47,52,57,58] showed that the collapse phase proceeds axisymmetrically even if the progenitor core is very rapidly spinning. They also found the development of nonaxisymmetric dynamics after bounce at low values of $T/|W|$ of $\sim$5–13% via a dynamical rotational shear instability [59,60].

Several 2D and 3D simulations of rapidly rotating core collapse included neutrino cooling and deleptonization in the postbounce phase via approximate leakage schemes [14,36,37,47,48] or multigroup flux-limited neutrino diffusion [13,15,61]. However, the effect of cooling/deleptonization on the nonaxisymmetric postbounce dynamics and associated GW emission was investigated only by Scheidegger *et al.* [47]. They found up to 10 times stronger GW emission if deleptonization/cooling was included. The influence of deleptonization and cooling on the earlier essentially axisymmetric dynamics and GW emission has not been addressed to date. Furthermore, the neutrino signature of rapidly rotating core collapse has been studied to date only on the basis of 1.5D (spherical symmetry plus approximate rotation) [62] that cannot account for the centrifugal deformation of the PNS and GW emission.

In this article, we present new results for the GW signature of rotating core collapse and first results on its early postbounce neutrino signature obtained from multi-D simulations. We study the dependence of collapse, bounce, and early postbounce evolution, GW and neutrino signal on precollapse rotation, progenitor structure and thermodynamics, and on the inclusion of deleptonization, neutrino cooling and heating in the early postbounce phase.

Our new results are based on a set of full GR simulations with our ZELMANI core-collapse simulation package, which is based on the open-source EINSTEIN TOOLKIT [63,64] and includes deleptonization during collapse and neutrino cooling, heating, and deleptonization after bounce via a three-species energy-averaged neutrino leakage scheme. Our simulations use the finite-temperature microphysical nuclear EOS of Lattimer and Swesty [65] with a choice of the nuclear incompressibility $K = 220$ MeV, which leads to cold neutron stars broadly consistent with current theoretical and observational neutron star mass and radius constraints (see, e.g., [66–68]).

We focus on the early postbounce evolution up to 25 ms after bounce which has been shown to proceed essentially axisymmetrically in rotating progenitors [47,52,57]. The ZELMANI simulations are carried out in 3D, but only in an octant of the 3D cube, using periodic (''rotating'' or ''$\pi/2$-symmetry'') boundary conditions on the $x-z$ and $y-z$ planes and a reflective boundary condition on the $x-y$ plane. This choice of ''octant-3D'' is appropriate for the collapse and essentially axisymmetric early postbounce phases (see [47,57,58]), allows for the development of 3D convective flows, but excludes the development of global low-m-mode nonaxisymmetric rotational dynamics. The latter could lead to strong elliptically polarized GW emission, possibly exceeding the linearly polarized signal from core bounce in emitted energy [28,47,55,57].

We simulate core collapse and early postbounce evolutions in a $12-M_\odot$ (at ZAMS) and in a $40-M_\odot$ (at ZAMS) presupernova stellar model, both drawn from the single-star solar-metallicity stellar evolutionary calculations of Woosley and Heger [69]. For each model, we carry out and compare results of six simulations, varying the precollapse rotation rate from zero to very rapid rotation. Every simulation is carried out once with postbounce neutrino leakage and once without for comparison. Rotation is set up by a rotation law that enforces near-uniform angular velocity in the inner core, as motivated by stellar evolutionary studies (e.g., [16]). In contrast to previous work that studied the progenitor dependence of collapse dynamics and GW signal [15,38,44], we set up our models to have approximately the same precollapse inner core angular momentum distribution as a function of enclosed mass coordinate,[1] rather than the same precollapse angular velocity or $T/|W|$, since the former is a conserved quantity while the latter two are useful parameters only when core structures (i.e., central density, compactness) at the onset of collapse are very similar, which generally is not the case and is certainly not the case for the $12-M_\odot$ and $40-M_\odot$ progenitors considered here.

Our simulations confirm previous results on the dependence of the GW signal on precollapse rotation (e.g., [14,43,44,47]), but we identify the excitation of nonlinear quadrupolar PNS pulsations at bounce in rapidly rotating cores. These pulsations occur around 700–800 Hz, last for many cycles and *our simulations show that they are clearly manifest in both the GW signal and the neutrino luminosities*.

We demonstrate that the dynamical effects of neutrino cooling and deleptonization and their impact on the GW signal of bounce and the very early postbounce evolution are tremendous at low rotation rates, but are strongly reduced with increasing rotation. This lends credence to previous work [14,43,44,47] that focused on the bounce and early postbounce GW signal of rapidly rotating core collapse.

We furthermore show that different rapidly rotating progenitors, if endowed with (approximately) the same angular momentum distribution in their inner 0.5–1$M_\odot$, will lead to the same late collapse, bounce, and early postbounce dynamics and associated GW signal, essentially independent of their precollapse structures and thermodynamics.

This paper is structured as follows: In Sec. II, we lay out our computational methods, input physics and GW extraction technique. In Sec. III, we discuss our model set and rotational setup. Section IV discusses our new result on correlated GW and neutrino signals from rapidly rotating

[1] In or near spherical symmetry, any quantity can be expressed as a function of radius r or enclosed baryonic mass M and the two are related by $dM(r) = 4\pi r^2 \rho(r) dr$.

collapse. We go into detail on the nature of the PNS pulsations, effects of neutrino leakage, and differences between simulations using the $12 - M_\odot$ and the $40 - M_\odot$ progenitor model in Secs. V A, V B, and V C, respectively. Section V D discusses the evolution of the rotation rate and prospects for nonaxisymmetric rotational instabilities in our simulated models. The detectability of the GW signals and of the high-frequency variations of the neutrino luminosity are assessed in Sec. V E. Finally, we summarize and conclude in Sec. VI.

II. METHODS

We use the ZELMANI GR core-collapse simulation package that is based on the open-source CACTUS COMPUTATIONAL TOOLKIT [70,71], the open-source CARPET adaptive mesh refinement driver, and the open-source EINSTEIN TOOLKIT [64]. In the following, we describe the various parts of ZELMANI that we use in this study.

A. Spacetime evolution and general-relativistic hydrodynamics

We evolve the full Einstein equations in a $3 + 1$ split (a Cauchy initial boundary value problem), using the BSSN formulation [72,73], a $1 + \log$ slicing condition [74] controlling the lapse function α, and a modified Γ-driver condition [75] for the coordinate shift vector β^i. The BSSN equations and the shift conditions are implemented in the code MCLACHLAN [76], which is part of the EINSTEIN TOOLKIT. The implementation makes use of fourth-order accurate finite differencing and details are given in [63,77].

For the evolution of the equations of GR hydrodynamics, we use the EINSTEIN TOOLKIT GR hydrodynamics code GRHYDRO [63], which implements the Valencia flux-conservative form of GR hydrodynamics (e.g., [78]) in the standard finite-volume high-resolution shock capturing approach. The equations are kept in semidiscrete form and first-order (in time) Riemann problems are solved at cell interfaces with the approximate Harten–Lax–van Leer–Einfeldt (HLLE) solver [79] on the basis of states reconstructed with the piecewise-parabolic method (PPM) [80] algorithm. High accuracy in time and coupling with the spacetime evolution is achieved via the Method of Lines [81] and fourth-order Runge-Kutta time integration. The time step is limited by the light crossing time and we use a Courant-Friedrichs-Levy factor of 0.4.

In simulations employing hot nuclear matter in nuclear statistical equilibrium, the electron fraction Y_e is the only compositional variable that must be tracked and the EOS is a function of rest-mass density ρ, temperature T (or specific internal energy ϵ), and Y_e. GRHYDRO solves an additional equation to advect the conserved scalar $\sqrt{\gamma}\rho Y_e$ [58], where γ is the determinant of the 3-metric.

GRHYDRO has undergone a rigorous set of standard tests [63]. A previous version of GRHYDRO has already been applied to stellar collapse with a finite-temperature nuclear EOS [57,58] and we have verified that the version used here reproduces previous results for the same set of input physics.

B. Adaptive mesh refinement and grid setup

We employ the CARPET adaptive-mesh refinement (AMR) driver [82] and perform our simulations in an octant of a 3D Cartesian cube, using periodic boundary conditions on two of the inner faces of the octant (implementing a $\pi/2$ rotational symmetry) and reflective boundary conditions on the equatorial plane. This limits 3D structure to spherical harmonic modes of even ℓ and m that are multiples of 4, which is not a significant limitation for the current study, since rotating core collapse and the very early postbounce evolution are likely to proceed nearly axisymmetrically [47,52,57].

CARPET implements Berger-Oliger-style AMR [83], where the fine grids are aligned with coarse grids, refined by factors of two. CARPET also implements subcycling in time, where finer grids take two time steps for every coarse grid step. The latter greatly improves efficiency, but also introduces significant complexity into the time evolution method. The refined regions can be chosen and modified arbitrarily.

In our baseline resolution, we employ eight levels of AMR in a box-in-box grid hierarchy, refining central regions where the highest resolution is required. The basegrid outer boundary is at 3400 km and at the onset of collapse, four levels of AMR (including the basegrid) are active. During collapse, we dynamically add additional finer levels, starting when the central density reaches 5×10^{10} g cm^{-3} and thereafter whenever the central density increases by a factor of 4. The finest refinement level has a linear resolution of $\sim$450 m and is set up to encompass the PNS after bounce, while we dynamically adjust the extent of the second-finest level (linear resolution $\sim$900 m) to always fully enclose the shock and provide constant high resolution for tracking the postshock flow. In addition to the baseline resolution, we perform higher-resolution simulations with $\sim$370 m linear resolution on the finest level for select models to test the resolution dependence of our results.

C. Equation of state

We employ the tabulated finite-temperature nuclear EOS by Lattimer and Swesty [65]. The Lattimer-Swesty (LS) EOS is based on the compressible liquid-droplet model. The transition from inhomogeneous to homogeneous nuclear matter is controlled by a Maxwell construction, and the nucleon-nucleon interactions are expressed in terms of a Skyrme model potential. The LS EOS comes with a nuclear symmetry energy of 29.3 MeV and has variants with an incompressibility of nuclear matter K of 180 MeV, 220 MeV, 375 MeV. The variant with $K = 180$ MeV yields a maximum cold neutron star mass

below that of the currently most massive known neutron star of $(1.97 \pm 0.04)M_\odot$ [84] and thus has been ruled out. We choose the variant with $K = 220$ MeV (LS220), since it is the EOS that is in best agreement with current theoretical and observational neutron star mass and radius constraints (e.g., [67,68]).

More details on the EOS table and on the implementation of the contribution of electrons, positrons, and photons, as well as other details of the construction of this EOS table are described in O'Connor and Ott [85]. Note that for the LS220 EOS, the Tolman-Oppenheimer-Volkoff (TOV) solution for a neutron star (NS) with $T = 0.1$ MeV in neutrinoless β-equilibrium yields a maximum gravitational (baryonic) NS mass of $\sim 2.04 M_\odot$ ($\sim 2.41 M_\odot$).

We point out that, although the properties of the EOS at supranuclear densities are poorly known and are model dependent, they are expected to have only a quantitative, but not a qualitative impact on rotating collapse, bounce, the early postbounce phase and on the associated GW signal [44]. Therefore, in this study, we limit the dimensionality of the explored input parameter space by using a single EOS.

D. Neutrino treatment

We employ the neutrino microphysics provided by the open-source code GR1D [2,85,86], which is available for download from [87]. This includes a parametrized $Y_e(\rho)$ deleptonization prescription proposed by Liebendörfer [88] during the collapse phase, a neutrino leakage scheme that approximates deleptonization, cooling, and heating in the postbounce phase, and contributions to the pressure from the presence of trapped neutrinos.

Liebendörfer's parametrized $Y_e(\rho)$ deleptonization prescription follows from the observation that the electron fraction during the collapse phase predicted from Boltzmann neutrino transport calculations is very well approximated as a function of density and shows only small variations with progenitor and EOS that have little impact on the dynamics [44,88]. More details on this scheme and the particular implementation we use can be found in [58,85]. Following [88], we employ an analytic fit, based on the $Y_e(\rho)$ profile previously used in [57,58], which was originally obtained for a $20 - M_\odot$ progenitor with the neutrino radiation-hydrodynamics transport code and neutrino microphysics of [89]. Details on this fit are available online [90]. We employ it for both our $12 - M_\odot$ and $40 - M_\odot$ progenitor models (see § III).

In the collapse phase of our simulations, we update the electron fraction in each zone according to the $Y_e(\rho)$ profile after each spacetime/hydro time step in an operator-split manner. We follow the prescription laid out in [88] for updating the specific entropy to account for thermalization of neutrinos at intermediate densities and to enforce constant entropy under Y_e changes at densities above 2×10^{12} g cm^{-3}, where we assume neutrinos to be trapped.

During the later stages of the collapse phase and throughout the postbounce phase, the trapped neutrinos exert a stress on the surrounding material. The effect of this neutrino stress on the hydrodynamics of core-collapse supernovae naturally arises when coupling the evolution of the neutrino fields to the matter; however, in our treatment of neutrinos we must explicitly take this term into account. At matter densities higher than the assumed trapping density, 2×10^{12} g cm^{-3}, we assume that the neutrinos behave as a relativistic ideal Fermi gas and approximate the stress based on the neutrino Fermi pressure gradient. The neutrino stress is then included as a source term in the GR hydrodynamics equations at each time-integration substep as detailed in [58] and the neutrino Fermi pressure is included in the stress-energy tensor.

Following core bounce, which we define as the time at which the entropy at the edge of the inner core reaches $3 k_B$baryon^{-1}, the simple $Y_e(\rho)$ prescription becomes inaccurate and cannot capture the effects of neutrino cooling, deleptonization, and neutrino heating. Hence, we switch to the leakage scheme of [85], which incorporates elements of previous work by [91,92]. We consider three neutrino species, ν_e, $\bar{\nu}_e$ and $\nu_x = \{\nu_\mu, \bar{\nu}_\mu, \nu_\tau, \bar{\nu}_\tau\}$. Neutrino pairs of all species are made in thermal processes of which we include electron-positron pair annihilation, plasmon decay [92], and nucleon-nucleon bremsstrahlung [86]. In addition, charged-current processes lead to the emission of ν_e s and $\bar{\nu}_e$ s.

The leakage scheme provides approximate energy and number emission rates based on local thermodynamics and an estimate of the energy-averaged optical depth τ_{ν_i} for each neutrino species. The latter requires a nonlocal calculation, which we implement in a ray-by-ray approach as schematically depicted by Fig. 1 and compute

$$\tau_{\nu_i}(r, \theta_l, \varphi_m) = \int_r^{R_{\max}} \sqrt{\gamma_{rr}} \bar{\kappa}_{\nu_i} dr'|_{\mathrm{ray}l,m}, \qquad (1)$$

where $\bar{\kappa}_{\nu_i}$ is the sum of the energy-averaged absorptive and scattering opacities for each neutrino species and γ_{rr} is the rr component of the 3-metric. A second such integral is computed with integrand $\chi_{\nu_i} = \kappa_{\nu_i}/\epsilon^2_{\nu_i}$, in which κ_{ν_i} is the sum of the energy-dependent absorption and scattering opacities. It is divided by its energy-dependent term, the square of the neutrino energy $\epsilon^2_{\nu_i}$. χ_{ν_i} is needed for computing the neutrino energy and number loss rates following [91].

The ray-by-ray approach, pioneered by [93] for flux-limited neutrino diffusion, has recently been employed in modern 2D neutrino radiation-hydrodynamics calculations (e.g., [3,4,24]) and in the 2D GR leakage scheme of [94]. It works well in situations that are spherical at lowest order like the one considered here. However, it is not appropriate for globally asymmetric systems, such as accretion disks around merged compact objects. In such situations it is necessary to evaluate the optical depth by integrating rays in various directions from each local emission region.

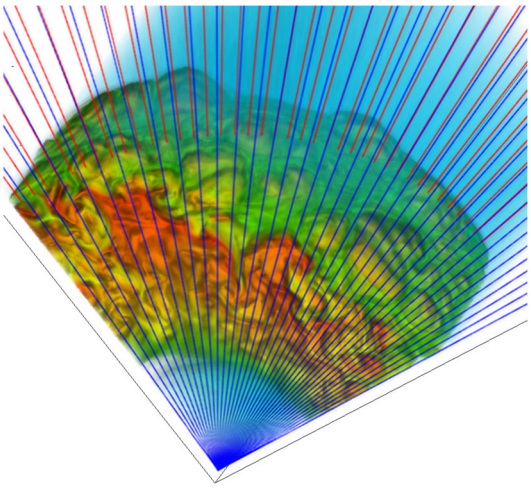

FIG. 1 (color online). Illustration of the rays along which calculations are performed for the neutrino leakage scheme. Shown here are two layers of rays overlaid on a volumetric visualization of a snapshot of the specific entropy distribution taken in the postbounce phase of model s12WH07j0. Light blue corresponds to low entropy ($0.6k_{\mathrm{B}}\mathrm{baryon}^{-1}$) and red corresponds to high entropy ($15k_{\mathrm{B}}\mathrm{baryon}^{-1}$).

In our simulations, we use 40 rays in latitude θ and 20 azimuthal rays in φ, covering $[0, \pi/2]$ in both angles as appropriate for the octant in which our simulations are performed. The radial resolution of the rays is 500 m out to 300 km and is logarithmically decreased further out. The outer radius for the ray calculation is set to 3000 km. We have studied variations in angular and radial resolution and find that the choices given here yield converged results.

Our 3D neutrino leakage calculation proceeds as follows: We interpolate density, temperature, Y_e, and the 3-metric from the 3D Cartesian grid onto the leakage rays and carry out a one-dimensional (1D) leakage calculation as described in [85] along each ray and for each neutrino species. This involves finding the optical depth τ_{ν_i} and the quantity χ_{ν_i} and, for each zone of the rays interior to the shock, computing the instantaneous number and energy leakage rates to obtain an approximate ''neutrino luminosity'' and mean energy as a function of radius and angle for each species.

The results of this calculation are then interpolated back onto our 3D Cartesian grid, where we locally compute the instantaneous number and energy leakage rates as well as the number and energy absorption rates computed on the basis of the interpolated approximate neutrino luminosity coming radially from below. In this approximation, we must attenuate the absorption rates with a term $\propto \exp(-\tau_{\nu_i})$ to avoid incorrect spurious heating at high optical depths [85].

All leakage calculations are carried out in operator-split fashion after the spacetime/hydro update and are first order in time, which we find to be sufficiently accurate given the small spacetime/hydro time step size. Updates are applied to the fluid rest-frame quantities, ignoring velocity dependence and other relativistic effects in consideration of the general approximate nature of the leakage scheme. In the highly dynamic first few milliseconds after bounce, we carry out all leakage calculations at every time step. Subsequently we switch to calculating the ray-by-ray calculations only every eight fine-grid time steps (corresponding to every 5×10^{-6} s) while continuing to evaluate the local expressions at every time step.

We have tested our 3D leakage scheme against the implementation in GR1D using a nonrotating model and found excellent agreement in the emitted luminosities, deleptonization, and cooling/heating rates in the early postbounce phase. The leakage scheme in GR1D itself has been compared with full multienergy neutrino radiation-hydrodynamics simulations and found to produce qualitatively robust results [2,85] with quantitative differences of order $\sim$20% across all transport variables.

E. Gravitational wave extraction and analysis

We employ the quadrupole formalism for extracting the GW signal from our simulations. We neglect higher spatial orders whose GW emission is suppressed by factors of $c^{-\alpha}$, $\alpha \geq 1$ and GW emission by anisotropic neutrino emission whose reliable prediction is not possible with the neutrino leakage scheme employed here.

The quadrupole formalism estimates the GW signal from the dynamical quadrupolar matter distribution alone. It does not take into account nonlinear curvature effects and is strictly valid only when the fields are weak $\frac{G}{c^2}\frac{R}{M} \ll 1$ and in slow motion $v/c \ll 1$.

Even though simple, comparison with curvature-based methods has proven the quadrupole formalism to be sufficiently accurate for the core-collapse scenario [77]. Most notably, it yields waveforms which are in good agreement (within a few percent) with those extracted at future null infinity $\mathcal{J}^+$ using the technique of Cauchy-characteristic extraction (e.g., [95]). It must be noted, however, that the quadrupole formalism breaks down in the context of black hole formation [96], when the matter has fallen inside the black hole and the GW signal is entirely due to (vacuum) black hole ringdown. This is not the case in our present study.

We estimate the GW strain by

$$h_{jk}^{TT}(t, \mathbf{x}) = \frac{2}{c^4}\frac{G}{D}\left[\frac{d^2}{dt^2} I_{jk}(t - D/c)\right]^{TT}, \tag{2}$$

where D is the distance to the source and

$$I_{jk} = \int \tilde{\rho}(t, \mathbf{x})\left[x_j x_k - \frac{1}{3}x^2 \delta_{jk}\right] d^3x \tag{3}$$

is the reduced mass-quadrupole tensor and the superscript TT denotes projection into the transverse-traceless gauge (see, e.g., [97]). The mass quadrupole is not uniquely defined in GR and the choice of density variable is ambiguous. Following previous work (e.g., [41,42,44,58]), we set

$\tilde{\rho} = \sqrt{\gamma} W \rho = \hat{D}$, because (i) this is the conserved density variable in our code, and (ii) $\sqrt{\gamma} d^3x$ is the natural volume element.

The reduced mass-quadrupole tensor can be computed directly from the computed distribution $\hat{D}(t, \mathbf{x})$. Numerical noise, introduced by the second time derivative of Eq. (3), may limit the accuracy of the result. We can circumvent this by making use of the continuity equation to obtain the first time derivative of Eq. (3) without numerical differentiation [98,99],

$$\frac{d}{dt} I_{jk} = \int \hat{D}(t, \mathbf{x}) \left[\tilde{v}^j x^k + \tilde{v}^k x^j - \frac{2}{3} (x^l \tilde{v}^l) \delta^{jk} \right] d^3x, \quad (4)$$

where we follow [100] and employ physical velocity components $\tilde{v}^i \equiv \{\tilde{v}_x, \tilde{v}_y, \tilde{v}_z\} \approx \{\sqrt{\gamma_{11}} v^1, \sqrt{\gamma_{22}} v^2, \sqrt{\gamma_{33}} v^3\}$ that are individually bound to $v < c$. This assumes that the 3-metric is nearly diagonal (which is the case in our gauge; see [77]). Also note that we have switched to contravariant variables in the integrand as these are the ones present in the code. This is possible since in the weak-field slow-motion approximation the placement of indices is arbitrary.

The two dimensionless independent GW strain polarizations h_+ and $h_\times$ incident on a detector located at distance D and at angular coordinate (θ, ϕ) in source coordinates are given by

$$h_+ - i h_\times = \frac{1}{D} \sum_{\ell=2}^{\infty} \sum_{m=-\ell}^{\ell} H_{\ell m}(t) {}^{(-2)}Y_{\ell m}(\theta, \phi), \quad (5)$$

where ${}^{(-2)}Y_{\ell m}$ are the spin-weighted spherical harmonics of weight -2 [101] and the $H_{\ell m}$ are expansion coefficients, which, in the quadrupole case, are related to the second time derivative of the mass-quadrupole tensor by

$$H^{\rm quad}_{20} = \sqrt{\frac{32\pi}{15}} \frac{G}{c^4} \left(\ddot{I}_{zz} - \frac{1}{2} (\ddot{I}_{xx} + \ddot{I}_{yy}) \right), \quad (6)$$

$$H^{\rm quad}_{2\pm1} = \sqrt{\frac{16\pi}{5}} \frac{G}{c^4} (\mp \ddot{I}_{xz} + i \ddot{I}_{yz}), \quad (7)$$

$$H^{\rm quad}_{2\pm2} = \sqrt{\frac{4\pi}{5}} \frac{G}{c^4} (\ddot{I}_{xx} - \ddot{I}_{yy} \mp 2i \ddot{I}_{xy}). \quad (8)$$

The rotating core-collapse models considered in this study stay almost perfectly axisymmetric in the collapse and early postbounce phases. In axisymmetry about the z axis, $I_{xx} = I_{yy} = -\frac{1}{2} I_{zz}$ and $I_{xy} = I_{xz} = I_{yz} = 0$. $h_\times$ vanishes and h_+ becomes

$$h_+ = \frac{G}{c^4} \frac{1}{D} \frac{3}{2} \ddot{I}_{zz} \sin^2\theta. \quad (9)$$

We will generally plot $h_+ D$ in units of centimeters when displaying gravitational waveforms.

The energy emitted in gravitational waves is given by

$$E_{\rm GW} = \frac{1}{5} \frac{G}{c^5} \int_{-\infty}^{\infty} dt \dddot{I}_{ij} \ddot{I}_{ij} dt = \frac{1}{5} \frac{G}{c^5} \int_{-\infty}^{\infty} dt [\ddot{I}^2_{xx} + \ddot{I}^2_{yy} + \ddot{I}^2_{zz} + 2(\ddot{I}^2_{xy} + \ddot{I}^2_{xz} + \ddot{I}^2_{yz})]. \quad (10)$$

In the special case of axisymmetry and in terms of $h_{+,e} = h_+ / \sin^2\theta$, this becomes

$$E^{\rm axi}_{\rm GW} = \frac{2}{15} \frac{c^3}{G^5} D^2 \int_0^{\infty} dt \left(\frac{d}{dt} h_{+,e} \right)^2. \quad (11)$$

The spectral GW energy density is given by

$$\frac{dE_{\rm GW}}{df} = \frac{2}{5} \frac{G}{c^5} (2\pi f)^2 |\tilde{\ddot{I}}_{ij}|^2, \quad (12)$$

so that

$$E_{\rm GW} = \int_0^{\infty} df \frac{dE_{\rm GW}}{df}. \quad (13)$$

In the above, we have introduced the Fourier transform of the mass-quadrupole tensor, $\tilde{\ddot{I}}_{ij}(f)$, and denoted it with a tilde accent.

In axisymmetry, the spectral GW energy density is related to $h_{+,e}$ by

$$\frac{dE^{\rm axi}_{\rm GW}}{df} = \frac{4}{15} \frac{c^3}{G} D^2 (2\pi f)^2 |\tilde{h}_{+,e}|^2. \quad (14)$$

When showing the spectral energy density, we will plot the dimensionless characteristic strain [102],

$$h_{\rm char}(f) = \sqrt{\frac{2}{\pi^2} \frac{G}{c^3} \frac{1}{D^2} \frac{dE_{\rm GW}(f)}{df}}, \quad (15)$$

which can be compared to the GW detector root-mean-squared noise,

$$h_{\rm rms}(f) = \sqrt{f S(f)}, \quad (16)$$

where $\sqrt{S(f)}$ is the one-sided detector noise amplitude spectral density in units of $(\mathrm{Hz})^{-1/2}$. For making rough statements about detectability, we use the single-detector optimal-orientation signal-to-noise ratio, which is given by

$$(\mathrm{SNR})^2 = \int_0^{\infty} d \ln f \frac{h^2_{\rm char}}{h^2_{\rm rms}}. \quad (17)$$

Note that we cut the calculation of integrals in the Fourier domain at 3000 Hz to filter out numerical high-frequency noise. Wherever we need $\sqrt{S(f)}$, we employ the projected broadband Advanced LIGO noise curve [the so-called zero-detuning, high-power configuration (ZD-HP)], available as file ZERO_DET_high_P.txt from [103].

For quantifying the difference between two gravitational waveforms $h_1(t)$ and $h_2(t)$, we introduce the mismatch [104,105],

$$\mathcal{M}_{\rm mis} = 1 - \mathcal{M}, \tag{18}$$

where $\mathcal{M}$ is the match, defined in terms of a maximization over time of arrival t_0 and GW phases ϕ_i of the two waveforms as

$$\mathcal{M} = \max_{t_0} \max_{\phi_1} \max_{\phi_2} \mathcal{O}[h_1, h_2], \tag{19}$$

where $\mathcal{O}[h_1, h_2]$ is the overlap, given by

$$\mathcal{O}[h_1, h_2] := \frac{\langle h_1|h_2\rangle}{\sqrt{\langle h_1|h_1\rangle\langle h_2|h_2\rangle}} \tag{20}$$

and where

$$\langle h_1|h_2\rangle = 4\,\mathrm{Re}\int_0^\infty df\,\frac{\tilde{h}_1(f)\tilde{h}_2^*(f)}{S_h(f)} \tag{21}$$

is the noise-weighted inner product. A mismatch of $\mathcal{M}_{\rm mis} = 0$ indicates that the two given waveforms are identical. Conversely, a mismatch of $\mathcal{M}_{\rm mis} = 1$ indicates that both waveforms are completely different. For calculating $\mathcal{M}_{\rm mis}$, we employ the PYGWDATAANALYSIS package [106], which is part of the EINSTEIN TOOLKIT.

III. INITIAL MODELS AND SETUP

A. Progenitor structure

We perform our collapse simulations with $12 - M_\odot$ and $40 - M_\odot$ (both at ZAMS) solar-metallicity presupernova stellar models evolved and provided to us by Woosley and Heger (2007) [69]. We refer to them as s12WH07 and s40WH07, respectively. Stellar winds lead to mass loss and at the onset of core collapse, defined as the time when the peak negative radial velocity exceeds 1000 km s^{-1}, model s12WH07 is a red supergiant with a final mass of $\sim 10.9 M_\odot$ and a radius of $\sim 4.4 \times 10^{13}$ cm ($\sim 630 R_\odot$). s40WH07 is a much more compact Wolf-Rayet star and has a radius of $\sim 8 \times 10^{11}$ cm ($\sim 10 R_\odot$) at a final mass of $\sim 15.3 M_\odot$. Dynamically relevant during collapse, though, are only the central regions and at the precollapse stage, s12WH07's central density, temperature, and entropy are $\sim 1.2 \times 10^{10}$ g cm^{-3}, $\sim 7 \times 10^9$ K, and $0.67 k_{\rm B}$ baryon^{-1}, respectively. Its iron core has an approximate mass of $1.3 M_\odot$ and a radius of ~ 1200 km. The spherical radius that encloses $1 M_\odot$ is ~ 634 km.

Model s40WH07's central structure is quite different at the precollapse stage. Its central density, temperature, and entropy are $\sim 2.2 \times 10^9$ g cm^{-3}, $\sim 8 \times 10^9$ K, and $1.08 k_{\rm B}$ baryon^{-1}, respectively. Its iron core has a mass of $\sim 1.8 M_\odot$ and an approximate radius of ~ 2200 km. The spherical radius that encloses the innermost $1 M_\odot$ of material is ~ 945 km.

Picking these two thermodynamically and structurally rather different models (cf. also Fig. 2) allows us to test if the systematics in the collapse dynamics, GW and neutrino signals that our simulations uncover are independent of thermodynamical and structural differences at the precollapse stage.

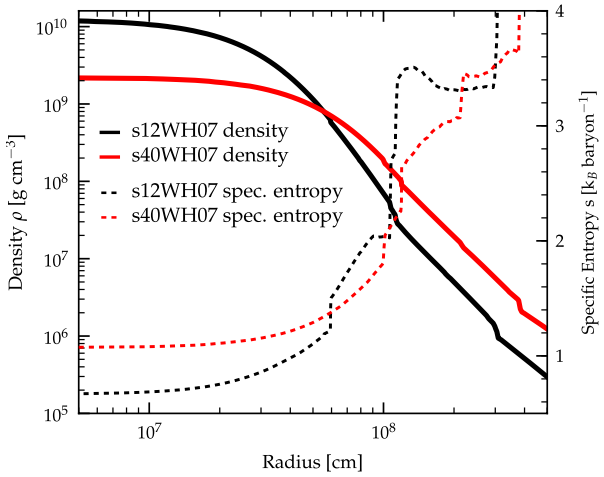

FIG. 2 (color online). Precollapse structure of the $12 - M_\odot$ (black graphs) and $40 - M_\odot$ (red graphs) progenitor models taken from [69]. Shown in solid lines is the radial density profile and dashed lines denote the radial entropy distribution as derived from our EOS. Note that, as expected from stellar evolution theory (e.g., [145]), the more massive progenitor has, at the onset of collapse, a lower central density, a higher central entropy, and a more extended core than its lower-mass counterpart.

We point out that both progenitor models considered here do not have the observational characteristics associated with long-GRB progenitor stars, which are expected to be rapidly spinning, low-metallicity, stripped-envelope or chemically homogeneous stars (e.g., [17]). However, stellar evolution theory has not yet converged on a robust prediction for the core structure and rotational configuration of long-GRB progenitors (see the discussion in [107]). Since the electron-degenerate iron cores of our two progenitor models have rather similar structure as many of the proposed long-GRB progenitors of [17], the results found for the current set of models are very likely to transfer to these models.

B. Rotational setup

Both model s12WH07 and model s40WH07 were evolved in a spherically symmetric stellar evolution code without rotation [69]. While a limited set of presupernova models with rotation is available (e.g., [16,17,108]), we choose to use nonrotating models and impose precollapse rotation by hand to study its effects during the collapse, bounce, and early postbounce phases in a controlled fashion.

We are interested in variations of the dynamics and the associated GW and neutrino signals that (1) arise from changes in the precollapse rotational configuration and (2) are a consequence of differences in the progenitor structure and thermodynamics. In the following, we describe the rotational setup that allows us to differentiate between the two.

According to the Poincaré-Wavre theorem (e.g., [109]) we expect the electron-degenerate iron cores [which are

essentially barotropic, $P \approx P(\rho)$] to have constant specific angular momentum $j = \Omega\varpi^2$ on cylindrical shells of distance ϖ from the rotation axis. We impose rotation using the rotation law [38,39]

$$\Omega(\varpi) = \Omega_{c,\mathrm{initial}}\left[1 + \left(\frac{\varpi}{A}\right)^2\right]^{-1}, \quad (22)$$

where $\Omega_{c,\mathrm{initial}}$ is the initial central angular velocity and the parameter A controls the cylindrical radius at which differential rotation becomes significant. This rotation law leads to constant specific angular momentum at $\varpi \gg A$.

We first set up rotation for model s12WH07 and choose $A = 634$ km, which corresponds to the spherical radius that encloses $1M_\odot$ at the precollapse stage. This yields an angular velocity profile that is consistent with results from stellar evolution calculations that include rotation [16,108] and ensures that the inner core is essentially uniformly spinning. Homologous collapse will preserve its nearly uniform rotation [15,107].

We vary the initial rotation rate by choosing the initial central angular velocity Ω_0 from the set $\{0, 1, 2, 4, 6, 8\}$ rad s^{-1}, which correspond to specific angular momenta j_∞ at infinity ranging from 0 to 3.2×10^{16} cm^2 s^{-1}. We enumerate models as s12WH07jn, where n ranges from 0 to 5, corresponding to the six choices of initial central angular velocity.

In order to isolate the influence of the progenitor star, we must compare simulations using the s12WH07 and s40WH07 progenitors that have identical or at least nearly identical angular momentum distributions. Since angular momentum is conserved per unit comoving mass, we compute the specific angular momentum on the equator (on the equator, the spherical radius r is equal to the cylindrical radius ϖ) of a given rotating s12WH07jn model as a function of enclosed mass $M(r = \varpi)$. We then take this specific angular momentum distribution and map it in mass coordinate to the equator of the corresponding s40WH07jn model and enforce constant angular velocity on cylinders $\Omega(\varpi) = j(M(r = \varpi))/\varpi^2$. With this approach, the equatorial regions (where $r \approx \varpi$) of both models have identical specific angular momentum as a function of enclosed mass. This mapping becomes, of course, more approximate at regions away from the equator. In principle, it would be possible to introduce an exact mapping $j(M, \theta)$ for enclosed mass at lateral angle θ, but this would violate the constraint of constant specific angular momentum on cylindrical shells, which we intend to adhere to in this study.

In Table I, we summarize key properties of our initial configurations. Since model s40WH07 is initially much more extended than model s12WH07 (see Fig. 2) it is initially much more slowly spinning. The rotational setup described in the above nevertheless yields integrated s12WH07 and s40WH07 angular momenta of the innermost $0.5M_\odot$ that agree within $\sim$12% at a given jn. The s40WH07jn models have systematically slightly less total angular momentum than their s12WH07jn counterparts at the same enclosed mass.

In addition to performing six simulations with varying initial rotation for each progenitor, we also repeat each simulation without neutrino leakage after core bounce. We append "nl" to these models (denoting "no leakage") and use them for comparison with our runs with leakage to assess the impact of neutrino leakage on the postbounce

TABLE I. Key initial model parameters for our simulations using the s12WH07 and s40WH07 progenitors. Models using the former progenitor are set up according to the rotation law specified in Eq. (22). Rotating s40WH07 models are set up to have the same specific angular momentum (in enclosed-mass coordinate) on the equator. Specific angular momentum is constant on cylindrical shells in both sets of initial models. j_∞ is the specific angular momentum at infinity. $\Omega_{\mathrm{c,initial}}$ is the initial central angular velocity. $J_{0.5M_\odot}$, $J_{0.6M_\odot}$, $J_{0.7M_\odot}$, and $J_{1M_\odot}$ are the total angular momenta within an enclosed-mass coordinate of (0.5, 0.6, 0.7, 1.0) $M_\odot$ respectively. $T/|W|_{\mathrm{initial}}$ is the initial ratio of rotational kinetic energy to gravitational energy as measured at a radius of 3400 km.

Model name	j_∞ (10^{16} cm^2 s^{-1})	$\Omega_{c,\mathrm{initial}}$ (rad s^{-1})	$J_{0.5M_\odot}$ (10^{48} g cm^2 s^{-1})	$J_{0.6M_\odot}$ (10^{48} g cm^2 s^{-1})	$J_{0.7M_\odot}$ (10^{48} g cm^2 s^{-1})	$J_{1M_\odot}$ (10^{48} g cm^2 s^{-1})	$T/\|W\|_{\mathrm{initial}}$ (%)
s12WH07j0	0.000	0	0.00	0.00	0.00	0.00	0
s12WH07j1	0.404	1	0.35	0.49	0.65	1.31	0.018
s12WH07j2	0.809	2	0.70	0.98	1.31	2.62	0.072
s12WH07j3	1.620	4	1.40	1.96	2.62	5.25	0.289
s12WH07j4	2.430	6	2.10	2.95	3.93	7.88	0.650
s12WH07j5	3.240	8	2.80	3.93	5.23	10.51	1.150
s40WH07j0	0.000	0.000	0.00	0.00	0.00	0.00	0
s40WH07j1	0.404	0.453	0.31	0.43	0.58	1.16	0.010
s40WH07j2	0.809	0.906	0.62	0.86	1.15	2.31	0.041
s40WH07j3	1.620	1.810	1.23	1.73	2.30	4.62	0.165
s40WH07j4	2.430	2.720	1.85	2.59	3.46	6.94	0.373
s40WH07j5	3.240	3.620	2.46	3.45	4.62	9.25	0.656

dynamics and the resulting GW signal. This allows us to quantify the systematic error in the waveform predictions of previous GR core collapse simulations without postbounce neutrino leakage (e.g., [44,46]).

C. Mapping and initial spacetime setup

We map the 1D progenitor models from 1D to 3D using linear interpolation and set up rotation by imposing constant angular velocity on cylindrical shells as discussed in the previous Sec. III B. We keep the mass distribution spherically symmetric when mapping and do not solve for rotational equilibrium, since this can be found consistently only for models with constant entropy and Y_e. The error introduced by not using models in rotational equilibrium is small, since collapse proceeds initially slowly, the region in sonic contact is large, and the core has sufficient time to adjust to the appropriate angular density stratification before the dynamical phase of collapse is reached [38,39].

We set up the initial 3-metric and the lapse function using the quasi-Newtonian spherically symmetric line element [97]. The extrinsic curvature and shift are set to zero on the initial slice. Since our precollapse configurations are essentially Newtonian, this yields accurate results and the 2-norm of the initial Hamiltonian (momentum) constraint violation is only of order 10^{-10} (10^{-11}).

IV. RESULTS: CORRELATIONS BETWEEN CORE DYNAMICS, GRAVITATIONAL WAVES, AND NEUTRINO SIGNALS

Our focus in this section is on the primary and most important new result of this study: the correlation of GW and neutrino signals in the very early postbounce evolution of rapidly rotating core-collapse supernovae. We use the s12WH07 model set with neutrino leakage as the basis of our discussion and postpone a detailed quantitative analysis of the effects of including neutrino leakage, differences due to progenitor structure, and various other aspects of our simulations to Sec. V.

Figure 3 depicts, for the s12WH07 model set, the central density (ρ_c) evolution, the GW signal, and the total approximate luminosities of the ν_e, $\bar{\nu}_e$, and ν_x neutrinos as predicted by our leakage scheme. The panels are ordered according to the initial rotation rate of each model from left to right and top to bottom. The times are given with respect to the times of core bounce in each model, which corresponds almost exactly to the time of the pronounced global maximum in ρ_c seen in the top subpanels of Fig. 3 in each model.

Neutrino leakage is activated at core bounce and we plot the resulting neutrino luminosities in the bottom subpanels of Fig. 3. The leakage scheme captures the large neutronization burst in the ν_e luminosity (L_{ν_e}), which reaches its peak within 5–8 ms of bounce. This burst sets in when the shock breaks through the ν_e neutrinosphere (the location where the optical depth $\tau_{\nu_e} \approx 2/3$) and electrons capture on protons freshly liberated from shock-dissociated heavy nuclei, producing electron neutrinos. The typical, much slower rise of the $\bar{\nu}_e$ and ν_x luminosities (e.g., [89]) is also present. The luminosities shown here are the instantaneous integral luminosities and we do not consider neutrino oscillations. Due to the approximate and energy-averaged nature of the leakage scheme, our quantitative predictions for the L_{ν_i} should be taken with a grain of salt, while their qualitative features are most likely robust [2,85]. We focus our discussion on the qualitative aspects of the neutrino signal.

The GW signals are shown in the center subpanels of Fig. 3. They are the waveforms observed by an observer located in the equatorial plane and their amplitudes have been rescaled by source distance D and are given in units of centimeters. In the nonrotating model s12WH07j0, GW emission is entirely due to prompt postbounce convection, which is driven initially by the negative entropy gradient that naturally develops behind the stalling shock, immediately after bounce. Prompt convection is seeded by perturbations coming from numerical noise in our simulations, which is, due to our Cartesian grid, of $\ell = 4$ (and even m) character. Hence, prompt convection has initially $\ell = 4$ structure and becomes visible in quadrupole GWs only[2] once $\ell = 2$ components develop in its nonlinear phase. GW emission sets in around 8 ms after bounce in model s12WH07j0, reaches peak amplitudes of $\sim$17 cm (corresponding to a dimensionless strain of $\sim 5.5 \times 10^{-22}$ at $D = 10$ kpc) and its GW spectral energy density peaks at $\sim$800 Hz. The onset of GW emission and the waveform characteristics sensitively depend on the shock dynamics, the thermodynamics of the region behind the shock, and on the distribution and magnitude of the seed perturbations (i.e., numerical resolution in our case). Hence, the GW signal observed for model s12WH07j0 is just one possible realization and should not be taken as being representative for prompt convection (see the discussion in [24,28]). The neutrino emission in the nonrotating model shows the global features generally seen in 1D (spherically symmetric) simulations (e.g., [85,89]). Besides that the GW and neutrino signals set in within milliseconds of each other, there is no other obvious correlation between them in model s12WH07j0 (other key quantitative results are summarized in Table II).

Rotation leads to a centrifugal flattening of the inner core into oblate shape, which results in a prominent spike in the GW signal at core bounce, when the inner core experiences extreme acceleration, essentially reverting its infall velocity on a time scale of $\mathcal{O}(1)$ ms. This bounce spike is clearly visible, though dwarfed by the signal from prompt convection, in the most slowly spinning model

[2]Accelerated $\ell = 4$ dynamics will also emit GWs, but their amplitudes are suppressed by c^{-2} compared to quadrupole ($\ell = 2$) waves [97].

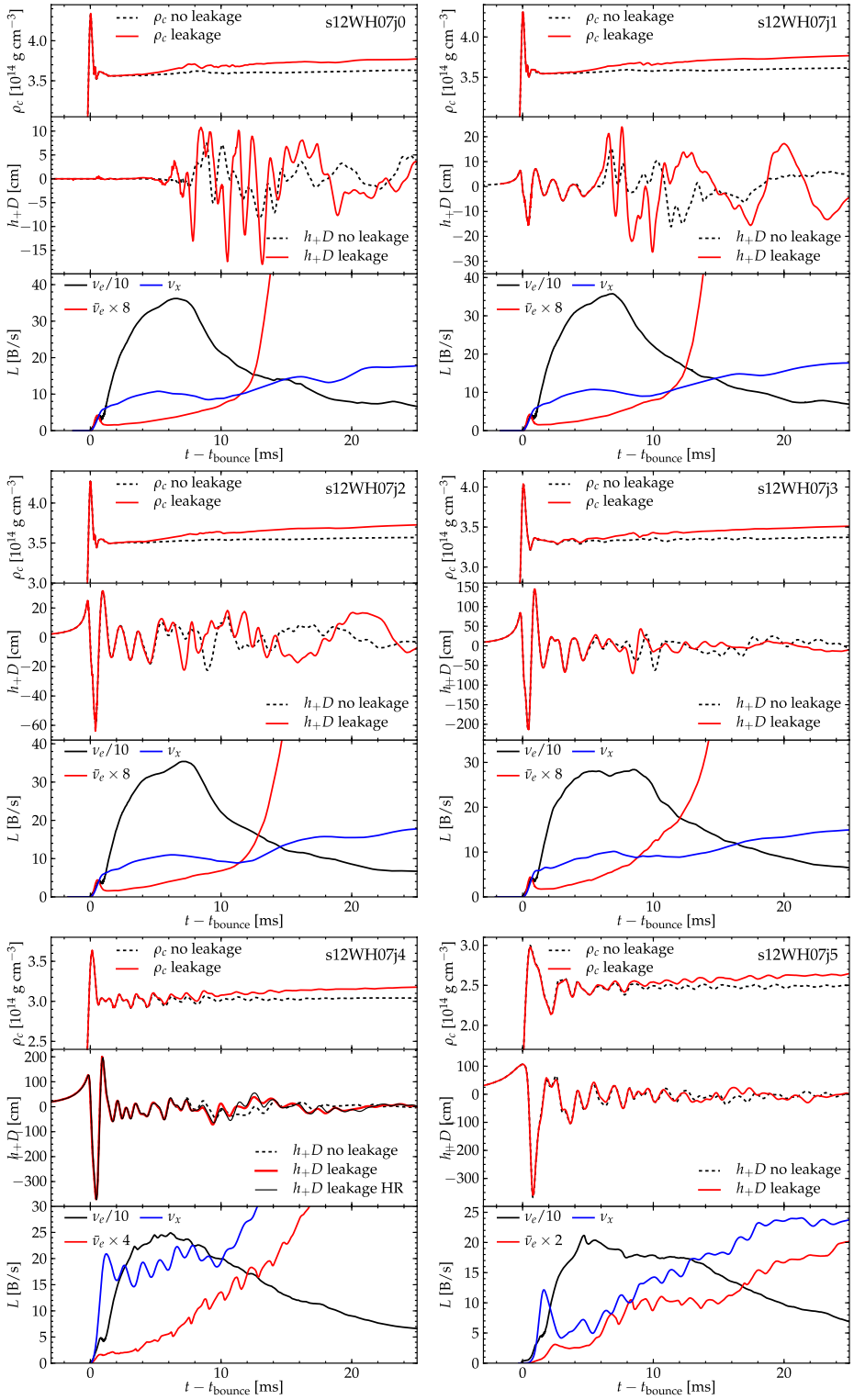

FIG. 3 (color online). Evolution of the central density (ρ_c, top subpanel), GW signal (h_+D, rescaled by distance D) seen by an equatorial observer (center subpanel), and ν_e, $\bar{\nu}_e$, ν_x neutrino luminosities L_{ν_i} (bottom subpanel) from shortly before core bounce to 25 ms after bounce in the s12WH07 models ordered according to their precollapse rotation rate (left to right, top to bottom). The L_{ν_i} are scaled to emphasize the very early postbounce phase. Also shown, in dashed lines, are the ρ_c evolutions and GW signals of the simulations without neutrino leakage. For the j4 model, we also plot the GW signal as obtained from a simulation with 20% higher resolution (HR). The effects of neutrino leakage on the dynamics and GW emission are strongest in nonrotating or slowly rotating models (j{0–2}). Note the prominent correlated oscillations in ρ_c, GWs, and neutrino signals starting, at low amplitude, in the j3 model and becoming quite prominent in the j4 and j5 models.

TABLE II. Summary of key simulation results for the s12WH07j{0–5} and s40WH07j{0–5} model sets. t_b is the time of core bounce, defined as the time at which the entropy reaches $3k_B$baryon^{-1} at the edge of the inner core, $\rho_{max,b}$ is the maximum density reached, $M_{ic,b}$ is the mass of the inner core at the point of maximum compression, $J_{ic,b}$ is the angular momentum contained in the inner core, $T/|W|_{ic,b}$ and $T/|W|_e$ are the ratios of rotational kinetic energy to gravitational energy at bounce and at 25 ms, respectively. The rightmost five columns contain key GW-related quantities: $|h_+|_{max}D$ is the magnitude of the peak GW amplitude, E_{GW} is the emitted energy in GWs, $h_{char,max}$ is the peak value of the characteristic GW strain spectrum [Eq. (15)] and $f_{char,max}$ is its location, and the optimal SNR in Advanced LIGO at 10 kpc is computed according to Eq. (17).

Model	t_b (ms)	$\rho_{max,b}$ (10^{14} g cm^{-3})	$M_{ic,b}$ ($M_\odot$)	$J_{ic,b}$ (10^{48} g cm^2 s^{-1})	$T/\|W\|_{ic,b}$ (%)	$T/\|W\|_e$ (%)	$\|h_+\|_{max}D$	E_{GW} ($10^{-9}M_\odot c^2$)	$h_{char,max}$ (10^{-22})	$f_{char,max}$ (Hz)	Optimal SNR in aLIGO at 10 kpc
s12WH07j0	178.52	4.34	0.56	0.00	0.0	0.0	17.5	0.27	9.0	802	6.02
s12WH07j0nl						0.0	8.2	0.04	3.8	871	3.07
s12WH07j1	179.60	4.33	0.57	0.44	0.4	0.4	25.5	0.51	12.2	730	12.10
s12WH07j1nl						0.3	15.6	0.17	9.4	738	6.61
s12WH07j2	182.93	4.28	0.57	0.91	1.6	1.3	60.3	1.58	28.5	750	15.37
s12WH07j2nl						1.3	59.6	1.36	21.3	736	12.97
s12WH07j3	198.40	4.04	0.59	1.82	5.1	4.9	209.6	20.08	75.0	716	40.75
s12WH07j3nl						4.6	209.0	19.65	83.3	721	41.19
s12WH07j4	235.63	3.64	0.62	2.88	9.2	9.5	363.5	47.13	121.6	787	66.22
s12WH07j4nl						8.9	363.4	46.47	117.2	771	65.14
s12WH07j5	383.36	3.00	0.66	4.42	13.6	13.8	346.3	23.03	86.1	754	73.42
s12WH07j5nl						12.4	353.3	24.32	92.0	737	73.64
s40WH07j0	418.22	4.41	0.62	0.00	0.0	0.0	41.4	0.03	7.1	381	9.81
s40WH07j0nl						0.0	16.8	0.07	3.8	711	4.74
s40WH07j1	419.93	4.40	0.62	0.54	0.4	0.5	41.5	0.53	14.4	769	10.17
s40WH07j1nl						0.5	27.7	0.23	8.2	607	12.95
s40WH07j2	425.22	4.32	0.62	1.06	1.4	1.8	67.9	1.64	26.4	711	16.41
s40WH07j2nl						1.7	67.2	1.60	23.0	677	16.15
s40WH07j3	448.23	4.10	0.67	2.34	5.0	6.2	237.2	23.16	93.4	708	47.70
s40WH07j3nl						6.2	235.9	22.41	96.4	689	46.83
s40WH07j4	495.68	3.65	0.68	3.38	8.9	11.6	367.0	45.94	131.9	766	75.35
s40WH07j4nl						11.1	366.8	45.09	137.2	757	73.78
s40WH07j5	591.19	3.00	0.72	4.89	12.6	14.7	402.8	30.20	87.3	743	86.24
s40WH07j5nl						13.1	383.4	26.07	85.7	716	85.12

s12WH07j1. It starts out with an initial period $P_0 = 2\pi$ s and makes a protoneutron star with a spin period of $\sim$10.2 ms and a ratio of rotational kinetic energy to gravitational energy ($T/|W|$) of $\sim$0.4%, which is a very small rotation rate in the context of rotating core collapse. Consequently, the overall collapse, bounce, and postbounce dynamics and the neutrino signals are very similar to the nonrotating case. However, the onset of appreciable GW emission already occurs robustly 5–8 ms before the peak of the ν_e neutronization burst and $\gtrsim$ 20 ms before the $\bar{\nu}_e$ and ν_x luminosities grow to their postbounce steady-state values.

Increasing precollapse core rotation results in a more oblate inner core at bounce, which translates directly into a more prominent bounce spike in the gravitational waveform. Model s12WH07j2 starts out with a central precollapse period of $P_0 = \pi$ s and is spun up by collapse to a postbounce period of $\sim$5.2 ms and a modest $T/|W|$ of $\sim$1.3%. Its inner core dynamics, diagnosed by ρ_c, and its neutrino luminosities are still very similar to the nonrotating case. Due to the increased oblateness of the inner core, the GW signal now has a peak amplitude of $\sim$60 cm (corresponding to $\sim 1.9 \times 10^{-21}$ at 10 kpc) and its dE_{GW}/df peaks at $\sim$750 Hz.

Model s12WH07j3 starts out with $P_o = \pi/2$ s and achieves a postbounce period of $\sim$2.4 ms and $T/|W|$ of $\sim$4.6%. It is the first model in this sequence that is appreciably affected by rotation: its maximum density at bounce is reduced by $\sim$10% due to the stabilizing centrifugal force and its peak GW amplitude is a factor of $\sim$3.5 greater than in model s12WH07j2. The maximum GW amplitude reached is $\sim$210 cm ($\sim 6.8 \times 10^{-21}$ at 10 kpc) and dE_{GW}/df peaks at $\sim$716 Hz. On the neutrino side, the rotationally deformed, less compact core, leads to a L_{ν_e} maximum that is significantly broadened, but reaches a lower maximum and settles at smaller postbounce values, which is consistent with what was found by Ott *et al.* [25] in 2D rotating core-collapse supernova simulations with

more accurate neutrino transport. The GW signal exhibits a number of pronounced postbounce oscillations due to pulsations of the PNS core whose radial components are reflected in small variations of ρ_c. The neutrino signals also exhibit slight traces of oscillations, though without clear correlation with ρ_c and GW signal.

Model s12WH07j4 (bottom left panel of Fig. 3) has a central precollapse spin period $P_0 = \pi/3$ s, a PNS spin period of $\sim$2 ms and an early postbounce $T/|W|$ of $\sim$8.9%. Its late collapse and bounce dynamics are affected by rotation, lowering the peak density at bounce by $\sim$20% compared to the nonrotating value, but still not significantly widening the bounce spike in the GW signal, which peaks at an amplitude of $\sim$364 cm ($\sim 1.2 \times 10^{-20}$ at 10 kpc). The spectral GW energy density $dE_{\rm GW}/df$ peaks at $\sim$787 Hz. This upward shift from model s12WH07j3 is due to the more pronounced and higher-frequency early-postbounce oscillations of the GW signal in this model. These oscillations in the GW signal are also prominently visible in its early-postbounce central density evolution. This suggests that a PNS pulsation mode has been excited and leads to global oscillations of the PNS core that persist at appreciable amplitude for $\gtrsim$ 20 ms after bounce (see Sec. VA for further analysis of the nature of this pulsation mode). The periodic contraction and expansion of the PNS core seen in model s12WH07j4 has a significant impact on the neutrino signal and leads to a characteristic modulation that is strongest in the $\bar{\nu}_e$ and ν_x luminosities and weaker in the ν_e luminosity.

To check the sensitivity of our results to resolution, we carry out another simulation of model s12WH07j4 with 20% higher resolution (HR). We find that the HR and standard-resolution GW signals (see Fig. 3) and all other quantities match almost perfectly until $\sim$10 ms after bounce. At later times, the damping of the PNS pulsations is slightly stronger in the lower-resolution calculation and resolution-dependent convective dynamics starts to play a role in the GW emission, thus leading to slight differences between the HR and standard-resolution simulations.

In Fig. 4, we present spectrograms obtained via short-time Fourier transforms of the central density (ρ_c), GW signal and ν_e, $\bar{\nu}_e$, and ν_x luminosities for model s12WH07j4. To guide the eye, we also plot the time series data for each spectrogram panel and add graphs of the corresponding energy- and angle-averaged neutrinosphere radii to the panels depicting neutrino luminosity data. There is a clear correlation between dynamics (ρ_c), GW signal, and neutrino signal: their power spectra all exhibit significant excess power at $\sim$700–800 Hz between $\sim$2 ms and $\sim$20 ms after bounce.

The $\bar{\nu}_e$ and ν_x neutrino luminosities exhibit variations of order $\lesssim$ 20%. Their emission occurs primarily below or near their neutrinospheres, so $L_{\bar{\nu}_e}$ and L_{ν_x} are particularly sensitive to their respective neutrinosphere radii (R_{ν_i}). As demonstrated by Fig. 4, the variations in R_{ν_i} due to the

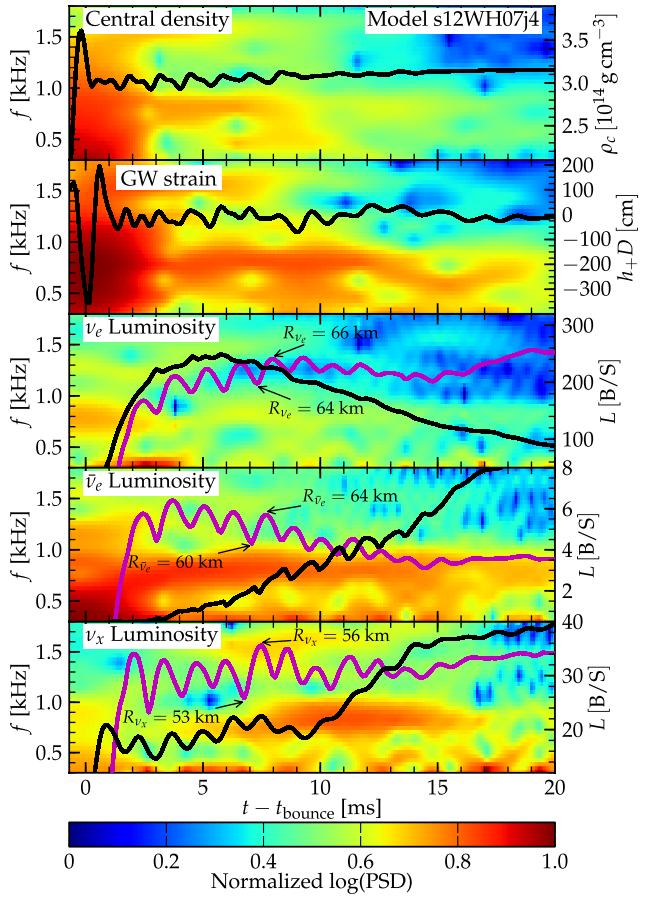

FIG. 4 (color online). Spectrograms of the power spectral densities computed via short-time Fourier transforms of the central density evolution (top panel), GW signal (second panel), L_{ν_e} (third panel), $L_{\bar{\nu}_e}$ (fourth panel), and L_{ν_x} (bottom panel). In each panel, the time-domain evolution of the respective quantity is superposed with the scales set by the right ordinates. In the panels showing neutrino luminosity data, we also provide graphs of the time evolution of the corresponding energy- and angle-averaged neutrinosphere radii. All quantities show significant correlated excess power in their power spectral densities (PSDs) around $\sim$700–800 Hz. The correlation in the ν_e luminosity is weak, since it is primarily sourced by electron capture outside the ν_e neutrinosphere. The spectrograms are obtained by sliding an 8-ms Hann window over the data with a 0.1 − ms time step. The scales on which the time series data are shown have been chosen to highlight the correlated multimessenger signal oscillations.

oscillations of the PNS core are sizable and have relative amplitudes of $\Delta R_{\nu_i}/R_{\nu_i} \sim 5\%$. They lead to a change of the neutrino-emitting volume of the same order and temporarily uncover regions of higher emissivity. This drives the variations in the $\bar{\nu}_e$ and ν_x luminosities. The ν_e luminosity, on the other hand, is due primarily to electron capture on free protons occurring above the neutrinosphere. Hence, L_{ν_e} is less affected by changes of its neutrinosphere's radius. Note that the neutrinospheres are centrifugally deformed and since we are plotting their

angle-averaged radii, we do not expect phase coherence between the L_{ν_i} and R_{ν_i} curves shown in Fig. 4.

The bottom right panel of Fig. 3 shows ρ_c, $h_+ D$, and L_{ν_i} for model s12WH07j5, our most rapidly spinning model. Its precollapse central spin period is $P_0 = \pi/4$s, which translates to an early postbounce spin period of $\sim$1.5 ms and a $T/|W|$ of $\sim$12.5%. The late collapse and bounce phase of this model is strongly affected by rotation and bounce occurs partially centrifugally at a central density of $\sim 3 \times 10^{14}$ g cm^{-3}. The strong influence of centrifugal effects slows down the late collapse and bounce of the inner core, which is reflected in the widening of the pronounced bounce peaks in ρ_c and in the GW signal. Model s12WH07j5's inner core quadrupole deformation is significantly greater than that of s12WH07j4's inner core. However, the rotationally slowed bounce dynamics and the resulting smaller net acceleration of the inner core leads to a peak GW amplitude of $\sim$346 cm ($\sim 1.17 \times 10^{-20}$ at 10 kpc), which is slightly smaller than in model s12WH07j4. Model s12WH07j5's GW spectral energy density $dE_{\rm GW}/df$ has a broad peak at 754 Hz with a FWHM of 60 Hz in the 720–780 Hz interval.

The central density evolution, GW signal, and neutrino luminosities of model s12WH07j5 show similar correlated behavior as in the less rapidly spinning model s12WH07j4: the postbounce central density evolution exhibits quasiperiodic oscillations that have appreciable amplitudes for many cycles, indicative of a PNS pulsation mode that is excited at core bounce and subsequently rings down. This dynamics is imprinted on GW and neutrino signals, which exhibit variations that correlate with the oscillations of the central density.

The correlated oscillations in central density, GW signal, and neutrino luminosities driven by rotationally excited pulsations are strong indicators of rapid rotation (at both precollapse and PNS stages) and the combined GW and neutrino data from the next galactic core-collapse event may thus allow one to constrain the rotation rate of its core. Provided the next galactic core-collapse supernova occurs sufficiently nearby, it will not only be possible to reconstruct its complete two-polarization GW signal but also to deduce detailed neutrino "lightcurves" and spectra from the events observed by neutrino detectors. Our present energy-averaged neutrino leakage scheme is too crude to make robust quantitative predictions on the expected neutrino signals. Qualitatively, however, we expect it to correctly capture the most important features and systematics. This includes the strong oscillations in the early $L_{\bar{\nu}_e}$ and L_{ν_x} evolutions going along with the PNS oscillations, but also the global trends with increasing rotation that one notes from Fig. 3 for all L_{ν_i}. Universally, increasing rotation leads to a decrease of L_{ν_e} and to a broadening of its early-postbounce peak. This change is small for models s12WH07j0 to s12WH07j2, but already significant in model s12WH07j3 and strong in models s12WH07j4 and s12WH07j5. The same systematics holds for the ν_x luminosities in our models. The $\bar{\nu}_e$ luminosity, on the other hand, exhibits an increase with rotation in the first 12–15 ms after bounce, which subsequently turns into a decrease with rotation at later times. This behavior is most likely due to the fact that the rotationally flattened neutrinospheres allow for greater early emission of $\bar{\nu}_e$ from small-radius polar regions at early times while the subsequent rise due to emission at greater radii is weaker in rapidly spinning models, since rapid rotation leads to uniformly lower temperatures (and entropies) [15,25].

V. RESULTS: DETAILED DISCUSSION

A. Analysis of postbounce core oscillations

The spectrograms of central density, GW signal, and neutrino luminosities of model s12WH07j4 shown in Fig. 4 all exhibit a strong long-lasting contribution at $f \sim$ 700–800 Hz. The extreme, quasidiscontinuous dynamics at core bounce inject power at a broad range of frequencies of $\sim$100– $\sim$ 2000 Hz, but within 2–3 ms after bounce the clear and persistent peak of the PSD at $\sim$700–800 Hz emerges and lasts for $\gtrsim$ 20 ms.

The pulsation is clearly of global nature, has significant amplitude out to $\gtrsim$ 60 km, and its oscillation period is of the same order as the dynamical time, $t_{\rm dyn} \sim (\bar{\rho} G)^{-1/2}$, of this region, suggesting that a pulsational eigenmode of the PNS has been excited. Moreover, we find a clear trend with increasing rotation (as is apparent even from the time-series data shown in Fig. 3). No oscillations are present in nonrotating or slowly rotating models (j0, j1, j2), but the moderately rapidly rotating j3 model and the rapid rotators j4 and j5 all exhibit the prominent oscillation mode at 700–800 Hz. This trend is independent of the progenitor model (see Sec. V C).

Rotation leads to a quadrupole deformation of the collapsing and bouncing inner core and the close connection of the appearance of the oscillation mode with rapid rotation strongly suggests that a quadrupole eigenmode is excited.

In nonrotating or only slowly rotating models, bounce is nearly spherical and most of the kinetic energy of the inner core is transferred to the nearly spherical hydrodynamic shock. In the case of rapid rotation, core bounce is nonuniform. In Fig. 5, we show colormaps of the specific entropy in the meridional plane of model s12WH07j4 at 0.25 ms and 0.64 ms after the entropy has first reached $3k_{\rm b}$/baryon, which is our criterion for core bounce. Velocity vectors and representative density isocontours are superposed. Due to the centrifugal deformation of the inner core, bounce occurs earlier and is stronger along the polar direction than in the equatorial plane. When the inner core begins to re-expand along the equatorial direction, it is already contracting again at the poles. This large-scale nonuniform dynamics acts as the initial perturbation exciting the pulsation of the newborn PNS.

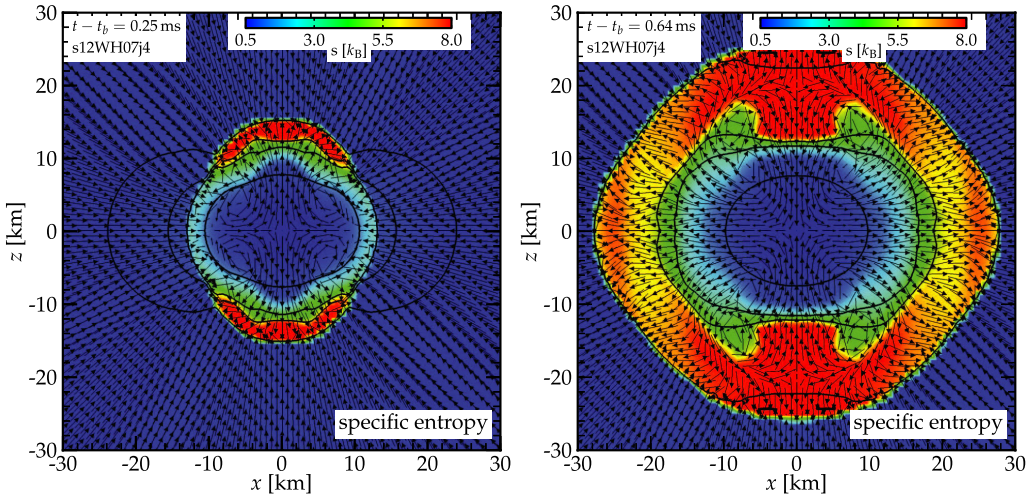

FIG. 5 (color online). Colormaps of the specific entropy in the meridional plane of the rapidly rotating model s12WH07j4. The contour lines mark isocontours of rest-mass density at $\{10^{14}, 10^{13}, 5 \times 10^{12}, 10^{12}\}$ g cm^{-3} (in this order from the origin). Velocity vectors are superposed and their length is saturated at $0.01c$. The left panel shows a snapshot at 0.25 ms after bounce while the right panel shows the situation at 0.64 ms. Due to rapid rotation and thus strong centrifugal support at low latitudes, bounce occurs earlier and is stronger (leading to higher specific entropies) near the poles. As shown in the left panel, at 0.25 ms after bounce, the inner core is re-expanding along the polar direction while most of the material near the equatorial plane is still falling in. At the slightly later time shown in the right panel, matter along the rotation axis is receding, while the inner core is expanding on the equator. The flow pattern in the inner core has strong quadrupolar features that excite the fundamental quadrupole oscillation mode.

Figure 5 also demonstrates that the velocity field of the inner core is primarily of quadrupole character and similar to the eigenfunction of the fundamental quadrupole mode (typically denoted by ^2f; c.f., Fig. 4.7 of [110]). This perturbation should predominantly excite the fundamental quadrupole mode of the star, which is then responsible for the dominant power at ~700–800 Hz observed in our rapidly spinning models (Fig. 4). To gain further confidence in this conclusion, we study a time sequence of the 2D meridional velocity field of model s12WH07j4. We remove the contribution from all frequencies by applying a bandpass filter on (800 ± 75) Hz and analyze the result. We find strong evidence for a velocity field akin to what has been found for the ^2f mode of nonrotating Newtonian stars (e.g., [111]) and rotating relativistic stars in the Cowling approximation [110,112]: (i) The radial velocity v_r does not exhibit any nodes in the PNS. (ii) $|v_r| \propto r$ in the same region, but with lateral dependence due to the oblate shape of the PNS. (iii) v_r along the polar axis and in the equatorial plane are out of phase by half a cycle. (*iv*) $v_\theta \propto \sin(2\theta)$ in the PNS. All of these features together are specific only to the fundamental quadrupole mode.

In Fig. 6 we show the time evolution of the filtered radial velocity along polar and equatorial directions at 0.45 km and 4 km from the origin. v_r along polar and equatorial directions at a given radius is out of phase by half a cycle, as expected for a ^2f oscillation. The variations in v_r are of order ~5% of the speed of light and, when compared with the typical speed of sound in the PNS (~0.15 c), clearly represent nonlinear pulsations. They are exponentially damped, most likely by the emission of sound waves.

The oscillations exhibited by our rapidly rotating models have manifestly nonlinear amplitudes and the excitation at bounce, while being primarily quadrupolar, involves large radial components and does not exactly match the eigenfunction of the pure ^2f mode. This leads to the excitation of a broad spectrum of other modes (see, e.g., [113]) as seen in the spectrograms of Fig. 4. In the linear regime, the ^2f mode does not modify the central density and should not

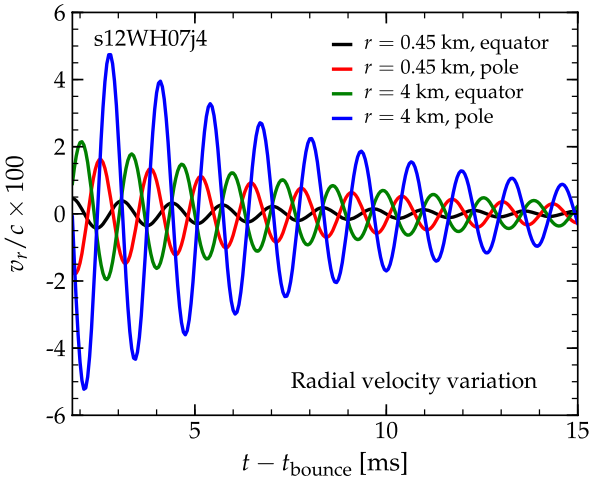

FIG. 6 (color online). The time evolution of the radial velocity of the PNS along polar and equatorial directions, bandpassed around the frequency of the leading peak of its oscillation spectrum, for model s12WH07j4. The radial velocity along polar and equatorial directions are out of phase by half a cycle at any given radius in the PNS interior. Such behavior is also exhibited by the ^2f mode of a nonrotating Newtonian star.

lead to the pronounced variations in the central density observed in our models. We attribute the presence of these variations to nonlinear driving of a quasiradial pulsation at the same frequency as the ${}^2f$ mode.

Finally, we note that the PNS oscillations in rapidly rotating models observed and investigated here are present also in the central density evolutions and GW signals in many models of previous parameter studies of rotating iron core collapse [38,39,41,44] and accretion-induced collapse of massive white dwarfs [46]. However, only the latter work made an effort to study these pulsations and first pointed out that fundamental quadrupole mode is likely to be the dominant mode of pulsation.

B. Leakage vs no leakage

All simulated models in this study are run twice: once with postbounce neutrino leakage and once without. In the collapse phase, the leakage and no-leakage (suffix "nl" in the model identifier) simulations are identical. After bounce, significant qualitative and quantitative differences develop, which we discuss in the following to gain an understanding of their relevance for early postbounce dynamics and the associated GW signals. This will also allow us to assess the error introduced by neglecting neutrino emission and deleptonization in the extensive previous parameter study of Dimmelmeier *et al.* [44]. We focus our discussion on the s12WH07j{0–5} model set. The effects of neutrino leakage are identical in models s40WH07j{0–5}.

The hydrodynamic shock wave, launched at core bounce, moves out in radius (and enclosed-mass coordinate) and dissociates infalling iron-group nuclei of the outer core into neutrons and protons. The degenerate electrons in the region behind the shock rapidly capture onto the liberated protons, dramatically decreasing Y_e and leading to the characteristic neutronization ν_e burst when the shock breaks out of the ν_e neutrinosphere. Nuclear dissociation and neutrino losses reduce the pressure behind the shock and decelerate its initially rapid expansion, eventually causing the shock to stall and turn into an accretion shock within tens of milliseconds of bounce. When neutrino leakage is not included, the shock still does work to break up heavy nuclei, but neutronization does not occur, the pressure behind the shock stays higher and the shock will stall at much larger radii. This is what we observe in our simulations. In Fig. 7, we present the time evolution of the shock position along the positive x axis for all models of the s12WH07j{0–5} set. In models with neutrino leakage, the shock reaches 90–130 km at 25 ms after bounce, while reaching 130–220 km in models run without neutrino leakage. We also note from Fig. 7 that rapidly rotating models tend to have larger equatorial shock radii (i.e., along the x axis in the figure) than their slowly and nonrotating counterparts. This is consistent with what was found by [15,25] and simply due to the rotational flattening

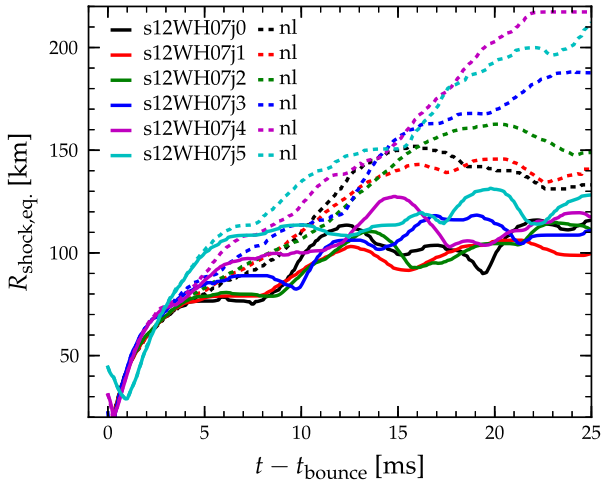

FIG. 7 (color online). Shock position on the equator (along the positive x axis) as a function of time after core bounce for the s12WH07j{0–5} model set. Models without neutrino leakage ("nl," dashed lines) reach significantly larger shock radii, since they are not, unlike the models that include neutrino leakage (solid lines), affected by neutrino cooling and deleptonization. The rapidly spinning models s12WH07j4 and s12WH07j5 show an initial transient decrease in their equatorial shock radii. This is due to shock formation occurring first at the pole while the equatorial regions of the inner core are still contracting. Note that the discrete shock radius data has been spline-interpolated to produce this plot.

of rapidly spinning cores. The polar shock radii of rapidly rotating models (not shown in Fig. 7) are correspondingly lower.

The top panels of Fig. 8 show colormaps of the Y_e distribution in the meridional plane at 25 ms after core bounce in the nonrotating model s12WH07j0 with neutrino leakage (left panel) and without (right panel). Fluid velocity vectors and isocontours of rest-mass density are superposed. In the simulation with neutrino leakage, the characteristic Y_e trough behind the shock and above the PNS core has clearly developed. In the PNS, at densities of $\gtrsim 5 \times 10^{12}$ g cm^{-3}, neutrinos are trapped and Y_e is essentially at its bounce value. It is only in this high-density region ($r \lesssim 20$ km) where the simulations with and without leakage agree in their Y_e distribution and structure. In the simulation with leakage, material is able to deleptonize, cool, and sink onto the PNS core, which makes it more extended, as shown by the 5×10^{12} g cm^{-3} and 10^{12} g cm^{-3} density isocontours that are at 3–5 km greater radii than in the simulation without leakage. At the same time, however, the overall region behind the shock is much more compact in the simulation with neutrino leakage: the 10^{11} g cm^{-3} isocontour and the shock, marked by the 10^{10} g cm^{-3} isocontour, are at ~10–15 km smaller radii.

The lower two panels of Fig. 8 show colormaps of the Y_e distribution at 25 ms after bounce in the meridional plane of the rapidly spinning model s12WH07j4 evolved with

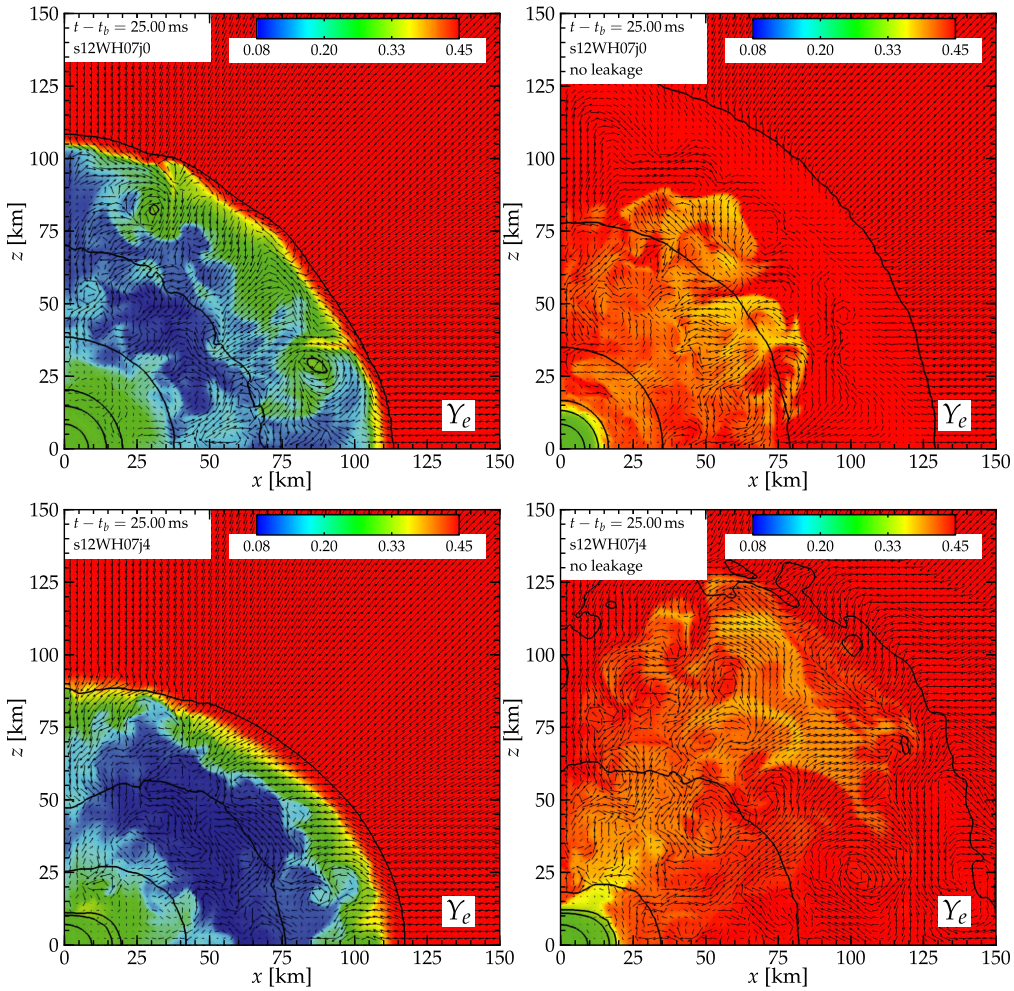

FIG. 8 (color online). Colormaps of the electron fraction Y_e in the meridional plane at 25 ms after bounce. The contour lines mark isocontours of rest-mass density (in this order from the origin) at $\{10^{14}, 10^{13}, 5 \times 10^{12}, 10^{12}, 10^{11}, 10^{10}\}$ g cm^{-3}. Velocity vectors are superposed and their length is saturated at $0.0125c$ to prevent the high collapse velocities of the outer core outside of the shock from cluttering the plot. The top panels show the nonrotating model s12WH07j0 evolved with postbounce neutrino leakage (left panel) and without (right panel). The bottom panels show the rapidly spinning model s12WH07j4 also with (left panel) and without neutrino leakage (right panel). The simulations with neutrino leakage show the characteristic depletion of Y_e due to electron capture in the region behind the shock. The shock is located at radii of ~110–120 km in the simulations with neutrino leakage, at ~125 km in the j0 model without leakage, and at ~160 km (~220 km) at the pole (equator) of the j4 model without leakage. In the PNS core, neutrinos are trapped and Y_e is at essentially its bounce value and only there the simulations with and without leakage yield the same Y_e and structure. The deleptonization and neutrino cooling in the runs with leakage significantly reduce the pressure behind the shock, lead to much smaller shock radii, and allow more material to pile up on the outer PNS core.

(left panel) and without (right panel) neutrino leakage. Comparing leakage and no-leakage results, we find the same general trends discussed for the nonrotating model in the above, but the differences are increased by rotation. The shock in the simulation without leakage has left the 150×150 km region of the frame, while it sits tight at small radii (~115 km at the equator and ~90 km at the pole) in the simulation with neutrino leakage. As in the nonrotating model, neutrino leakage allows material to cool, deleptonize, and sink to smaller radii, leading to an extended high-density region at the edge of the PNS core also in model s12WH07j4.

The top and center subpanels of each model panel in Fig. 3 depict the postbounce central density evolution and GW signal in each model, respectively. The results obtained with neutrino leakage are shown in solid lines while the no-leakage results are plotted as dashed curves. Independent of rotation rate, the central density of models run with neutrino leakage exhibits a secular upward trend due to the contraction of the PNS core as more deleptonized material settles onto it. In the simulations without leakage, material behind the shock cannot cool and deleptonize and does not settle onto the PNS, whose postbounce central density stays practically constant.

In the GW sector, the differences between simulations with and without leakage vary strongly with increasing rotation. In order to quantify the differences in the GW signals extracted from simulations with and without neutrino leakage, we compute their mismatch as defined by Eq. (18). The mismatch is 0 for identical waveforms and 1 if the waveforms have nothing in common. The mismatch measure adopted here and discussed in Sec. II E weights the Fourier-space representations of the waveforms (for a source at 10 kpc) with aLIGO detector sensitivity and thus emphasizes differences relevant to aLIGO observations. We note that variations in the waveforms due to different wave extraction methods alone lead to mismatches of order 10^{3}–10^{-2} [77]. However, if all waveforms are extracted with the same technique, as is the case here, the mismatch should be a meaningful quantity.

In the nonrotating model s12WH07j0, the GW signal is due exclusively to prompt convection. Prompt convection and the associated GW signal are strongly modified by deleptonization and neutrino cooling, which add lepton gradients and reduce the physical extent of the convection zone. This leads to a stronger, higher-frequency GW signal from prompt convection in the model evolved with neutrino leakage. We compute (and record in Table III) a mismatch of 0.51 between the GW signals from the leakage and no-leakage simulations. While this mismatch is large, we point out that the GWs from prompt convection seen in the simulations presented here are just example realizations of GWs from prompt convection and are not representative for the entire range of possible GW signals from this process. Variations in progenitor core structure, thermodynamics, and precollapse perturbations that seed convection may lead to large qualitative and quantitative variations in the GW signal from prompt convection (see, e.g., the discussion in [28]) that could easily dwarf the difference between the leakage and no-leakage variants that we see in our models.

With increasing rotation, the overall GW signature gradually becomes dominated by the dynamics of the centrifugally flattened inner core, which turns into the core of a nascent protoneutron star after bounce. Neutrinos are trapped in the inner core and diffuse out on much longer time scales than simulated here. Hence, the parts of the GW signal due to inner core dynamics should be nearly identical in leakage and no-leakage simulations. This is what we find already in the slowly spinning model s12WH07j1 (top right panel of Fig. 4), whose GW signal is dominated by the inner core in the first $\sim$5 ms after bounce. Evaluated at this time, the mismatch of leakage and no-leakage GW signal is only of order 10^{-3}. Subsequently, prompt convection takes over, leading to a mismatch of 0.66 at the end of the simulation. With further increasing rotation, the signal due to the inner core's bounce becomes globally dominant and the total (i.e., for the entire waveform) mismatch decreases to 0.53 (s12WH07j2), 0.13 (s12WH07j3), 0.06 (s12WH07j4), and 0.03 (s12WH07j5). Most of the mismatch is built up at times $\gtrsim$ 5 ms after bounce, when the shock has broken out of all neutrinospheres and when the large GW signal due to inner core dynamics has sufficiently died down for the aspherical flow in the semitransparent region behind the shock to play an appreciable role in the GW emission.

When considering the mismatch in the first 5 ms after bounce only, we note somewhat different systematics. The mismatch is large in the nonrotating model, small for the slowly to moderately rapidly spinning models, and increases again for the most rapidly spinning model s12WH07j5 (the same systematics holds for the s40WH07j{0–5} models; see Table III). We attribute this to the strong global rotational deformation of the most rapidly spinning model. It leads to shock formation, propagation, and strong neutrino emission from polar regions milliseconds before the shock forms at the equator. This results in an earlier onset of differences between leakage and no-leakage simulations.

TABLE III. Mismatch of GW signals of simulations with and without postbounce neutrino leakage computed according to Eq. (18) for an event at 10 kpc. The mismatch is provided for the signal up to 5 ms, 10 ms, and 25 ms after bounce.

Model	Mismatch $<$5 ms	Mismatch $<$10 ms	Mismatch $<$25 ms
s12WH07j0nl/s12WH07j0	3.7×10^{-1}	3.5×10^{-1}	5.1×10^{-1}
s12WH07j1nl/s12WH07j1	1.3×10^{-3}	5.2×10^{-1}	6.6×10^{-1}
s12WH07j2nl/s12WH07j2	1.6×10^{-3}	2.1×10^{-1}	5.3×10^{-1}
s12WH07j3nl/s12WH07j3	4.6×10^{-4}	5.8×10^{-2}	1.3×10^{-1}
s12WH07j4nl/s12WH07j4	1.3×10^{-4}	1.4×10^{-2}	5.9×10^{-2}
s12WH07j5nl/s12WH07j5	1.0×10^{-3}	2.4×10^{-3}	2.8×10^{-2}
s40WH07j0nl/s40WH07j0	3.8×10^{-1}	1.4×10^{-1}	3.9×10^{-1}
s40WH07j1nl/s40WH07j1	3.6×10^{-4}	4.6×10^{-2}	5.8×10^{-1}
s40WH07j2nl/s40WH07j2	3.2×10^{-4}	4.2×10^{-2}	4.7×10^{-1}
s40WH07j3nl/s40WH07j3	9.9×10^{-5}	6.3×10^{-3}	5.3×10^{-2}
s40WH07j4nl/s40WH07j4	1.6×10^{-4}	4.0×10^{-3}	5.9×10^{-2}
s40WH07j5nl/s40WH07j5	2.3×10^{-3}	6.0×10^{-3}	2.4×10^{-2}

C. Influence of progenitor structure

In the discussion up to now, we have relied exclusively on our s12WH07j{0–5} model set that uses the $12 - M_\odot$ (at ZAMS) progenitor model of [69]. We turn now to comparing these simulations with the s40WH07j{0–5} model set that uses the $40 - M_\odot$ (at ZAMS) progenitor of the same study. As discussed in Sec. III B, we have chosen a procedure for imposing rotation that leads to approximately the same specific angular momentum as a function of enclosed mass of inner core material for s12WH07 and s40WH07 models of the same jn parameter. In particular, our procedure ensures that at a given rotational setup jn, the s40WH07jn model will have approximately the same or less, but never more angular momentum than the s12WH07jn model.

We first turn our attention to the nonrotating (j0) models. Model s12WH07j0 experiences bounce at 178.5 ms after the start of the simulation, reaches a peak density of 4.3×10^{14} g cm^{-3}, and has an inner core mass at bounce ($M_{\rm ic,b}$) of $\sim 0.56 M_\odot$. The core of the $40 - M_\odot$ progenitor of model s40WH07j0 starts to collapse at a central density that is ~5.5 times lower than s12WH07j0's and, according to the free-fall estimate, we expect its collapse time to be ~2.3 times longer. Model s40WH07 indeed reaches core bounce at 418.2 ms, which is almost exactly what our estimate predicts. The central density at bounce is 4.4×10^{14} g cm^{-3}. This is slightly higher than the value of model s12WH07j0 and we attribute this to model s40WH07j0's greater $M_{\rm ic,b}$ of $\sim 0.62 M_\odot$. The difference in $M_{\rm ic,b}$ is due to s40WH07j0's higher initial core entropy (see Sec. III A and [114]), since both models are using the same $Y_e(\rho)$ prescription for deleptonization in the collapse phase. In a full neutrino radiation-hydrodynamics simulation, one would expect additional differences due to progenitor-dependent variations in deleptonization [44].

In the top left panel of Fig. 9 we compare the late collapse and early postbounce evolutions of the central density and of the GW signal in models s12WH07j0 and s40WH07j0. Modulo minute deviations and despite not insignificant differences in precollapse structure and

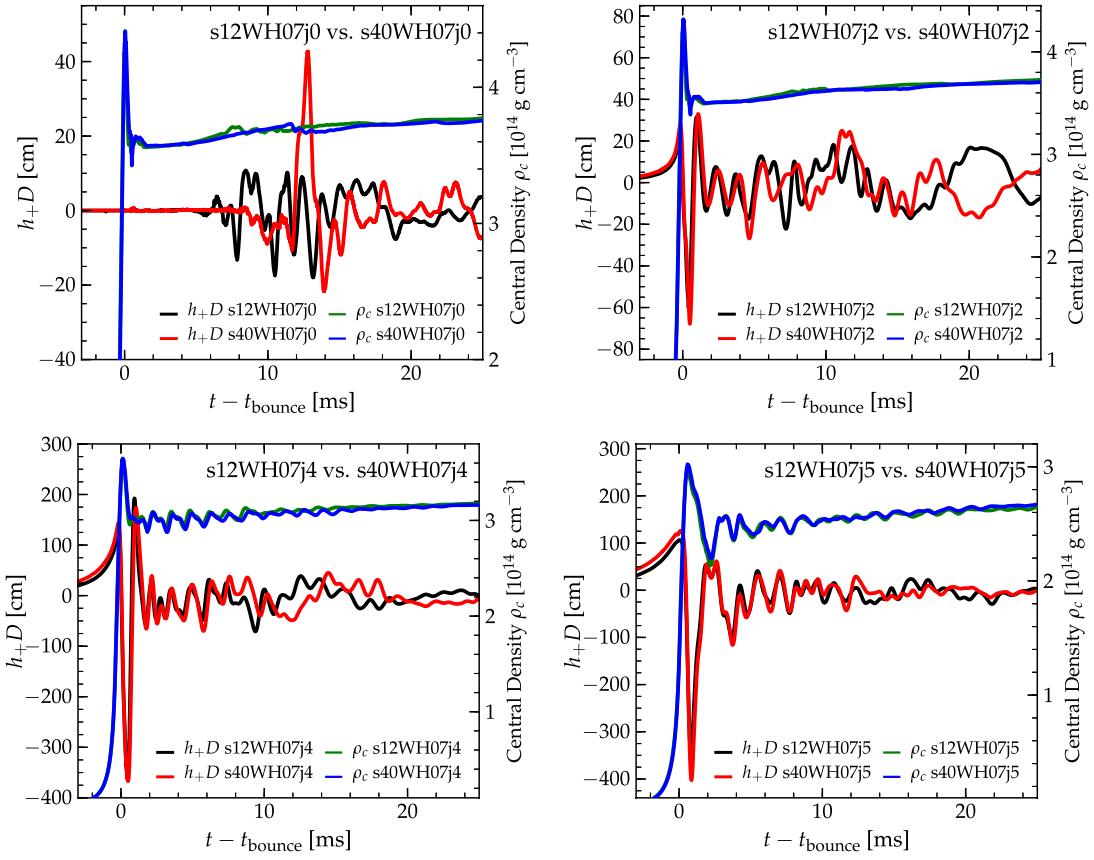

FIG. 9 (color online). Comparison of select models of the s12WH07 model set (using the $12 - M_\odot$ progenitor) with their s40WH07 counterparts (using the 40-$M_\odot$ progenitor). Shown are the evolution of the GW signal seen by an equatorial observer (left ordinate) and of the central rest-mass density (right ordinate). The GW signal h_+ is rescaled by source distance D and plotted in units of centimeters, the central rest-mass density ρ_c is given in units of 10^{14} g cm^{-3}, and the time is measured in milliseconds relative to the time of core bounce in each model. The central density evolutions in all s12WH07 and s40WH07 models are extremely close to one another. The GW signals of the nonrotating models (top left panel) differ significantly. However, with increasing rotation (from left to right, top to bottom), the dominant parts of the GW signal grow very similar.

TABLE IV. Mismatch of GW signals of simulations using the s12WH07 and the s40WH07 progenitor model computed according to Eq. (18) for an event at 10 kpc. The mismatch is provided for the signals up to 5 ms, 10 ms, and 25 ms after bounce.

Model	Mismatch <5 ms	Mismatch <10 ms	Mismatch <25 ms
s12WH07j0/s40WH07j0	4.1×10^{-1}	3.2×10^{-1}	5.8×10^{-1}
s12WH07j1/s40WH07j1	1.9×10^{-2}	5.6×10^{-1}	6.9×10^{-1}
s12WH07j2/s40WH07j2	3.1×10^{-2}	2.4×10^{-1}	6.5×10^{-1}
s12WH07j3/s40WH07j3	1.1×10^{-2}	8.8×10^{-2}	1.6×10^{-1}
s12WH07j4/s40WH07j4	1.9×10^{-2}	7.6×10^{-2}	2.0×10^{-1}
s12WH07j5/s40WH07j5	1.2×10^{-2}	1.7×10^{-2}	5.2×10^{-2}

thermodynamics, the central density evolutions of the two models practically lie on top of each other. The situation is different for the GW signals. In both models, GW emission is due to prompt convection, which is highly sensitive to bounce dynamics, progenitor thermodynamics, and seed perturbations and is generally of stochastic character (e.g., [24,28,115]). Hence, given the differences in inner core mass and core thermodynamics, the large difference that we find in the GW signals from prompt convection in these models is not surprising. Using our mismatch measure [Eq. (18)] we find a mismatch of 0.58 for the GW signals of models s12WH07j0 and s40WH07j0 in the first 25 ms after bounce. More data on their mismatch are summarized in Table IV while key quantitative results are provided in Table II.

With increasing rotation, the dynamics of the centrifugally deformed inner core begins to dominate the GW signal and a prominent characteristic peak develops whose shape and magnitude depends to very good approximation only on mass and angular momentum of the inner core [44,46]. This simplifies the signal and drives the GW signals of the two model sets to congruence.

The top right panel and the two bottom panels of Fig. 9 compare s12WH07 and s40WH07 models with j2, j4, and j5 rotational setup. Models with j1 and j3 are omitted for clarity, but show no special behavior. The close qualitative and quantitative agreement in the central density evolutions found for the nonrotating case is unchanged by rotation. On the other hand, the effect of rotation on the differences between the GW signals is remarkable, in particular when one focuses on the signal up to 5 ms after bounce. Taking the signals up to this point and computing the mismatch, we find 0.41 for the nonrotating models, and 0.019, 0.031, 0.011, 0.019, and 0.012 for j1, j2, j3, j4, and j5, respectively. Thus even the slightest bit of rotation already has a unifying effect and drives down the mismatch to the percent level about which it hovers, affected primarily by slight, but not negligible differences in the bounce peak and in the first few postbounce oscillations. When considering the entire GW signal out to the end of our simulations at 25 ms after bounce, the mismatch is significantly larger (see Table IV), since the GW emission begins to be significantly affected by prompt convection outside the PNS core starting at 5–10 ms after bounce.

It is interesting to compare some of the key representative quantities summarized in Table II between the s12WH07j{0–5} and s40WH07j{0–5} models. Rotation leads to an increase of the inner core mass at bounce ($M_{\rm ic,b}$; e.g., [44]). In the s12WH07 model set, $M_{\rm ic,b}$ increases from $\sim 0.56 M_\odot$ for j0 to $\sim 0.66 M_\odot$ for j5. The s40WH07 progenitor model's higher-entropy inner core is more massive, its mass is $0.62 M_\odot$ in j0 and increases to $0.72 M_\odot$ in j5. The s40WH07j{1–5} models have less angular momentum as a function of enclosed mass (see Table I), but their inner cores, due to their greater mass, contain up to $\sim 15\%$ more angular momentum at bounce ($J_{\rm ic,b}$) than the inner cores of the s12WH07j{1–5} models. These differences in $M_{\rm ic,b}$ and $J_{\rm ic,b}$ lead to quantitative changes at the same or lower level in the maximum density at bounce, the maximum GW signal amplitude, the peak of the GW energy spectrum, and the values of $T/|W|$ obtained at bounce: s40WH07 models (i) undergo bounce at $\lesssim 3\%$ greater central densities, (ii) reach maximum GW signal amplitudes $|h_+|_{\rm max} D$ that are $\lesssim 15\%$ greater, (iii) have peaks of their $dE_{\rm GW}/df$ that are at $\lesssim 5\%$ smaller frequencies, and (iv) assume maximum values of $T/|W|$ that are $\lesssim 10\%$ smaller than in their s12WH07 counterparts. These results are readily explained by considering that the inner cores of the s40WH07 models are slightly less compact (very similar ρ_c at greater $M_{\rm ic,b}$ and $J_{\rm ic,b}$) than their s12WH07 counterparts. The lower compactness leads to a lower value of $T/|W|$ (at fixed J, $T \propto R^{-2}$ and $|W| \propto R^{-1}$), but to a greater quadrupole moment, varying at a just slightly slower rate, resulting in a slightly higher $|h_+|_{\rm max} D$.

In Fig. 10 we plot $dE_{\rm GW}/df$ spectra comparing results from s12WH07 and s40WH07 models with no rotation (j0; top panel), moderate rotation (j2; center panel), and rapid rotation (j5; bottom panel). As expected from the large differences in the time domain seen in the top left panel of Fig. 9, the spectral GW energy densities of models s12WH07j0 and s40WH07j0 are quite distinct. Slow rotation already leads to many common features and the spectra of rapidly spinning models are nearly identical.

The correlations between dynamics, gravitational waveforms, and neutrino signals described in Sec. IV for the s12WH07j{0–5} model set also exist in very similar fashion in the s40WH07j{0–5} models. For the central density

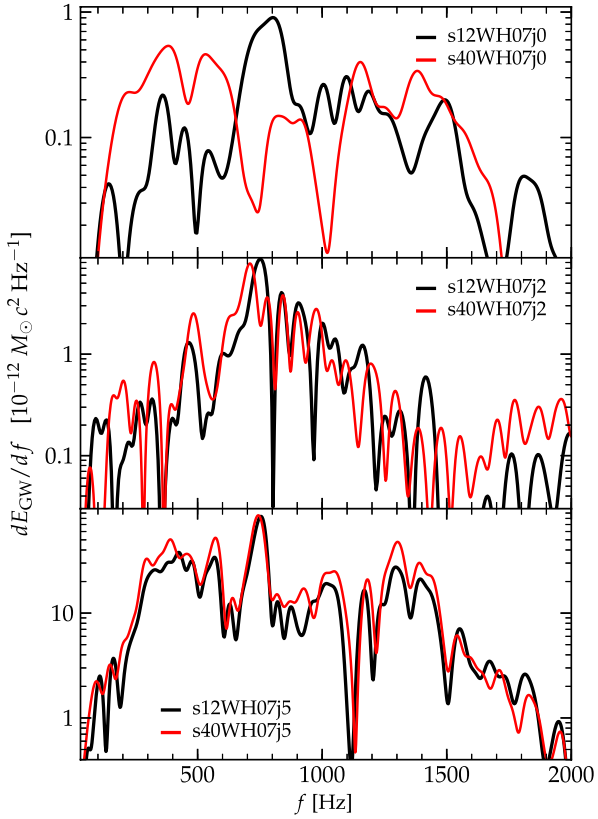

FIG. 10 (color online). Comparison of the spectral GW energy densities [$(dE_{GW}/df$; Eq. (14)] of select models using the $12-M_\odot$ and the $40-M_\odot$ progenitor at the same precollapse rotation rate. Top panel: Nonrotating case (j0); the spectra vary greatly. Center panel: Moderate rotation (j2); the spectra exhibit many similar features. Bottom panel: Rapid rotation (j5); the spectra are nearly identical.

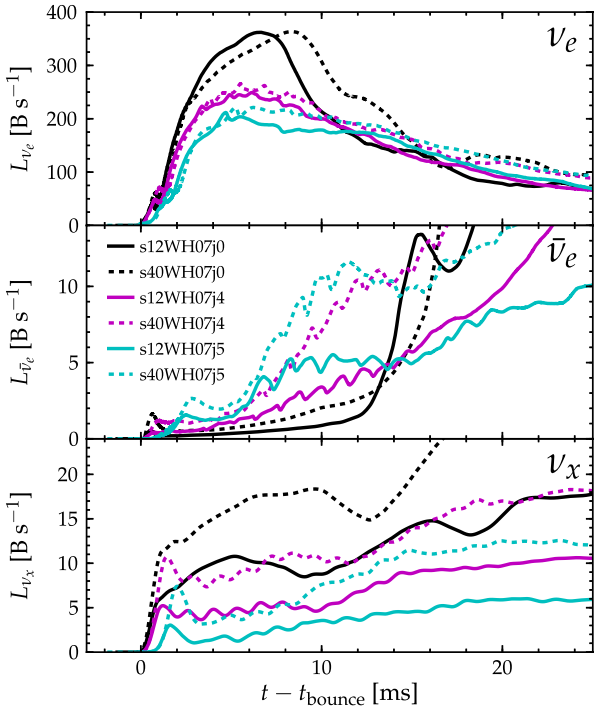

FIG. 11 (color online). Comparison of the approximate ν_e (top panel), $\bar{\nu}_e$ (center panel), and ν_x (bottom) luminosities in models s12WH07j0, s12WH07j4, s12WH07j5 (all solid lines) with their s40WH07j0, s40WH07j4, s40WH07j5 counterparts (all dashed lines). The vertical scales have been chosen to emphasize the oscillations observed primarily in $L_{\bar{\nu}_e}$ and L_{ν_x} of the rapidly spinning j4 and j5 models. While quantitative aspects should be regarded as approximate, one notes that the s40WH07 models have systematically larger early postbounce luminosities than their s12WH07 counterparts.

evolution (a proxy for the core dynamics) and GW signal, this is already apparent from the two rapidly rotating cases shown in the bottom panels of Fig. 9 in which the s40WH07 models essentially mirror the evolution of their s12WH07 counterparts. Figure 11 compares the approximate ν_e (top panel), $\bar{\nu}_e$, and ν_x luminosity evolutions of j0 (black curves), j4 (magenta curves), and j5 (cyan curves) variants of s12WH07 (solid lines) and s40WH07 (dashed lines). The characteristic oscillations that go along with the quadrupole PNS pulsations seen in models s12WH07j4/j5 also occur in their s40WH07j4/j5 counterparts. While our leakage scheme permits us to make only approximate quantitative predictions, we do find interesting systematic trends when comparing the neutrino luminosities of s12WH07 and s40WH07 models. The rise times of the ν_e luminosity are similar in both progenitors, but the peaks are broader in the s40WH07 models, most likely because bounce is stronger, leading to somewhat larger shock radii and more dissociated material for electrons to capture on at early times. The $\bar{\nu}_e$ emission is primarily thermal at early times and the ν_x emission is completely thermal; hence, for these neutrino species, the hotter cores of s40WH07 models exhibit systematically higher luminosities than their cooler s12WH07 counterparts. We expect these more qualitative than quantitative trends to carry over to future full energy-dependent neutrino radiation-hydrodynamics simulations, which will be needed for reliable quantitative estimates.

D. Evolution of the rotation rate and prospects for rotational instability

Rotating core collapse proceeds axisymmetrically even in very rapidly spinning cores (see, e.g., [47,57,58]). After bounce, nonaxisymmetric dynamics will naturally develop as a consequence of convection in the region behind the shock and above the PNS core. The latter, however, may become rotationally unstable to the growth of nonaxisymmetric modes that could lead to global deformation and extended quasiperiodic elliptically polarized GW emission [28,47,55,57] that could surpass the linearly polarized emission from core bounce in total emitted energy. Such nonaxisymmetric rotational instability has been identified to come in three flavors:

(a) At $T/|W| \gtrsim 27\%$, a dynamical purely hydrodynamic instability will deform a spheroidal self-gravitating fluid body into ellipsoidal ($m = 2$, barlike) shape (e.g., [116]).

(b) At $T/|W| \gtrsim 14\%$, the same kind of deformation may be driven by the presence of a dissipative process (e.g., viscosity or GW backreaction [117,118]). The growth time scale for this secular instability is likely to be of order seconds or longer [119,120].

(c) A dynamical shear instability may operate on the free energy stored in differential rotation, leading to nonaxisymmetric spiral modes that redistribute angular momentum. This kind of instability is common in accretion disks (e.g., [121] and references therein) and has been shown to occur also in differentially rotating neutron star models already at values of $T/|W|$ of order $\sim 1\%$ [59,122–125]. Hence, this instability is commonly referred to as low-$T/|W|$ instability. While the inner PNS core is likely to be uniformly spinning, differential rotation naturally develops in the outer core (e.g., [15,107]) and full 3D simulations [47,52,57] have found the instability to occur in PNSs with a $T/|W|$ in the range of ~ 5–13%. The detailed conditions necessary for its development and its potential interaction with other processes, e.g., the magnetorotational instability [9], operating on differential rotation remain to be fully explored (but see [60]).

The simulations presented in this paper are carried out in an octant of the 3D cube, and thus do not allow the development of the typically unstable $m = \{1, 2, 3\}$ nonaxisymmetric modes. While we cannot track this low-order nonaxisymmetric dynamics, it is still interesting to consider the rotational configuration of our postbounce models to assess the potential for development of nonaxisymmetric rotation dynamics in the postbounce epoch. Previous estimates have been based on 1.5D (spherical symmetry plus angle-averaged rotation) GR simulations [2], 2D Newtonian simulations with multigroup flux-limited diffusion neutrino transport [15], or on 2D GR simulations that did not include deleptonization and neutrino cooling after bounce [44,46], so it is worthwhile to reconsider the question at hand.

In Fig. 12, we show the evolution of $T/|W|$ from shortly before bounce to 25 ms after bounce for all rotating models and for simulations with and without neutrino leakage. As expected from the discussion in Sec. V C, the only difference between models using the s12WH07 and the s40WH07 progenitor is that the latter models reach slightly lower peak and postbounce $T/|W|$.

All models reach their peak $T/|W|$ at bounce and settle at a ~ 10–30% lower early postbounce $T/|W|$ (see Table II for quantitative details). The $T/|W|$ evolutions in initially slowly to moderately rapidly rotating models (j1–j3) show

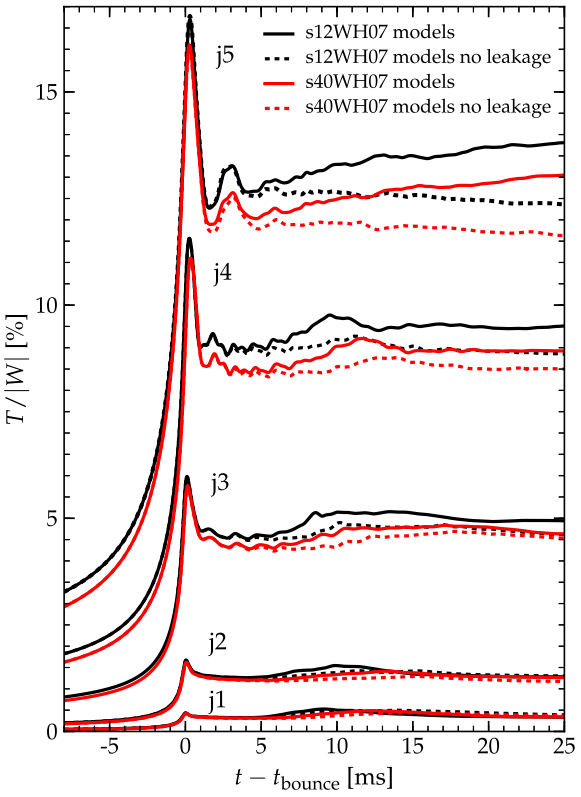

FIG. 12 (color online). Rotation rate $T/|W|$ as a function of time after bounce for the rotating models of the s12WH07 (black lines) and s40WH07 (red lines) model sets. Results for simulations with (solid lines) and without (dashed lines) neutrino leakage are shown. s12WH07 and s40WH07 models show qualitatively and quantitatively very similar $T/|W|$ evolutions. s40WH07 models, which are endowed with slightly less angular momentum than their s12WH07 counterparts, have slightly lower $T/|W|$ (see Tables I and II). In rapidly rotating models, neutrino leakage leads to a more rapid contraction and spin-up after bounce than predicted by models without leakage. Nonaxisymmetric instability at low $T/|W|$ is likely to occur in models with j3, j4, and j5 rotation. The j5 models may even reach the threshold of 27% for the high-$T/|W|$ dynamical instability within a few hundred milliseconds of bounce.

little dependence on progenitor or neutrino leakage and $T/|W|$ remains almost constant in their postbounce evolutions. This is different in the rapidly spinning j4 and j5 models. In simulations with neutrino leakage, accreting, high-angular momentum material can efficiently cool, deleptonize, settle, and add spin to the PNS. Hence, one observes a significant postbounce increase of $T/|W|$ from its value immediately after bounce to the end of the simulation. This is not the case in simulations without leakage and $T/|W|$ may even slightly decrease after bounce, since only low-angular momentum from polar regions quickly reaches small radii.

The models with precollapse rotation choices j3, j4, and j5 have early postbounce $T/|W|$ of $\sim 4.5\%$, $\sim 9\%$, and $\sim 12.5\%$. Consistent with previous results [15,44,107],

their PNS cores are approximately uniformly spinning, but the angular velocity begins to fall off roughly proportional to $r^{-\alpha}$ with $\alpha \sim 1.3$–1.7 at radii $\gtrsim 10$–20 km. Hence, these models are likely to be subject to the low-$T/|W|$ instability [44,47,52,57].

When linearly extrapolating the postbounce $T/|W|$ growth in the j5 models under the simplifying assumption that the angular momentum of the accreting material is approximately constant in time, we find that a $T/|W|$ of 27%, the approximate threshold for the guaranteed dynamical bar-mode instability, is reached at $\sim$300 ms after bounce. Even if accretion stops, cooling and contraction of the PNS to final NS form will likely lead to $T/|W|$ in excess of the dynamical instability threshold in the j5, j4, and even in the j3 models (see, e.g., the mapping of initial core spin to final NS spin in [15]), unless angular momentum is being redistributed or radiated by some other mechanism, e.g., the low-$T/|W|$ instability, the secular instability, or MHD processes.

E. Notes on detectability

1. Gravitational waves

In the rightmost five columns of Table II, we summarize key quantities describing the GW emission characteristics of the simulated models: the peak of the GW signal amplitude time series ($|h_+|_{\max} D$) as seen by an equatorial observer rescaled by distance D, the emitted energy in GWs ($E_{\rm GW}$), the peak value of the dimensionless characteristic strain [($h_{\rm char,max}(f)$; Eq. (14)] in frequency space and at an equatorial observer location of 10 kpc, the frequency $f_{\rm char,max}$ at which $h_{\rm char,max}$ is located, and the single-detector Advanced LIGO optimal signal-to-noise ratio (SNR) as calculated using Eq. (16) for a core collapse event at 10 kpc, the fiducial galactic distance scale. Since we are considering linearly polarized signals in h_+, for nonoptimal orientation the SNR will scale $\propto \sin^2\theta$, where θ is the angle between observer line of sight and the rotation axis of the collapsing star.

In the following, we focus exclusively on the physically more realistic models that include neutrino leakage. Furthermore, as discussed in Sec. V C, the $12 - M_\odot$ and the $40 - M_\odot$ progenitors lead to very similar GW emission in the phases that we simulate and we do not discuss them separately.

The peak GW signal amplitudes of our models lie in the range $20\ {\rm cm} \lesssim |h_+|_{\max} D \lesssim 400\ {\rm cm}$, which corresponds to $7 \times 10^{-22} \lesssim |h_+|_{\max} \lesssim 1.3 \times 10^{-20}$ at 10 kpc and is fully consistent with the results of [44], who also focused on the linearly polarized GW signal from core bounce and early postbounce evolution, but did not include postbounce neutrino leakage. The lowest peak amplitudes are reached in nonrotating (j0) or slowly rotating (j1) models, in which the emission is primarily due to prompt convection. The highest amplitudes are emitted by the most rapidly spinning models (j4 and j5). A further increase of precollapse rotation would not result in significantly higher peak amplitudes, since j5 models are already strongly affected by centrifugal effects, which reduce the acceleration the inner core is experiencing at bounce, and thus lead to lower GW amplitudes when rotation begins to dominate the dynamics.

The total energy emitted in GWs is in the range $2.7 \times 10^{-11} M_\odot c^2 \lesssim E_{\rm GW} \lesssim 4.7 \times 10^{-8} M_\odot c^2$. Again the nonrotating and slowly rotating models mark the lower end of this range. The upper end is set by the j4 models, since the j5 models, due to the strong influence of rotation, have more slowly varying waveforms and lower $E_{\rm GW}$ [($E_{\rm GW} \propto \int (dh/dt)^2 dt$; Eq. (11)].

Comparing our model predictions with GW detector sensitivity is done best in the frequency domain. In Fig. 13 we contrast $h_{\rm char}(f)$ spectra of our s12WH07j{0–5} model set with the projected noise levels in Advanced LIGO [in the zero-detuning, high-power configuration [103]; (aLIGO ZD-HP)], KAGRA/LCGT [126], and Advanced Virgo (AdV) in a potential wideband configuration [127]. Shown are the one-sided detector noise amplitude spectral densities $\sqrt{S(f)}$ in units of ${\rm Hz}^{-1/2}$ and $h_{\rm char} f^{-1/2}$ of our models [the $f^{-1/2}$ rescaling is introduced to conform to the units of $\sqrt{S(f)}$], assuming a source distance of 10 kpc. $h_{\rm char}$ peaks in a narrow frequency range of about 700–800 Hz for all rotating models. Slowly spinning models typically have their $h_{\rm char}$ peak at the high end of this range and the frequencies of their spectral peaks are influenced primarily by the properties of the nuclear EOS (not studied in detail here; see [44]). Very rapidly spinning models tend towards the lower end and develop strong low-frequency components, which almost reach the level of the peak around 750 Hz in model s12WH07j5.

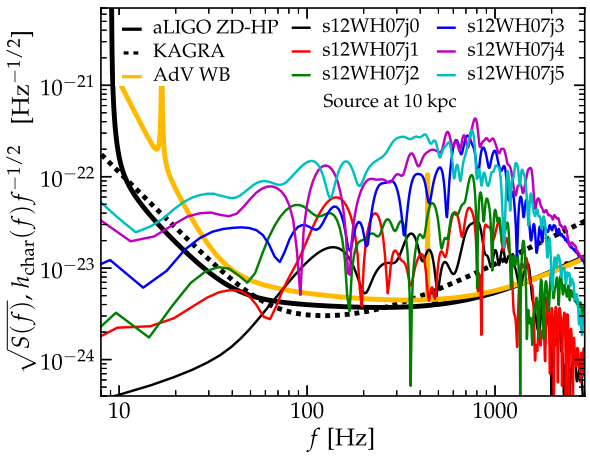

FIG. 13 (color online). Comparison of projected Advanced LIGO broadband [zero-detuning, high-power (aLIGO ZD-HP)] [103], KAGRA/LCGT [126], and potential Advanced Virgo wideband (AdV WB) [127] sensitivity with the characteristic GW amplitudes $h_{\rm char}(f) f^{-1/2}$ of the s12WH07j{0–5} model set at a source location of 10 kpc.

The $h_{\rm char}$ spectra of all models shown in Fig. 13 have large portions that lie above the detector noise levels. By integrating the ratio $h^2_{\rm char}(f)/(fS(f))$ over frequency [Eq. (17)] and using $S(f)$ of Advanced LIGO in ZD-HP mode [103], we arrive at single-detector optimal (i.e., most optimistic) SNRs at an assumed distance of 10 kpc that range from ~6 for the nonrotating model j0 to ~73 for the most rapidly rotating model j5. While these numbers appear large and suggest that Advanced LIGO-class detectors may be able to detect the emitted waveforms, we emphasize their "optimal" nature: a real astrophysical core-collapse event is highly unlikely to be optimally oriented and optimally located on the sky with respect to a detector or a network of detectors on Earth (see, e.g., [128] for a discussion of sky coverage for detector networks). Furthermore, the noise in interferometric GW detectors is typically non-Gaussian and nonstationary, and detection may be further complicated by noise artifacts ("glitches") that were found in first-generation detectors (e.g., [129]). These artifacts may be present also in the detectors of the advanced generation considered here. The SNR of a real signal above which one may be confident of a detection is typically assumed to be $\gtrsim 8$ for Gaussian noise and at least two detectors observing the event in coincidence [130]. For real noise even higher SNRs may be required and the exact threshold will depend on the detector network, data quality, and search methodology.

In addition to the general question of detectability, one may ask: (1) Would advanced GW detectors be able to observe the pronounced postbounce variations in the GW signal of rapidly rotating models that are correlated with variations in the neutrino luminosity? (2) Would advanced GW detectors be sensitive to effects of neutrino leakage in the very early postbounce phase out to 25 ms simulated for our models? (3) Will advanced GW detectors be able to tell the difference between rotating core collapse in a $12-M_\odot$ and in a $40-M_\odot$ progenitor with the same angular momentum distribution?

A fully reliable answer to these questions would require a Bayesian model-selection/parameter-estimation approach as taken by [32,34]. The answer to (1) is most likely "yes" for events taking place in the Milky Way, since the GW signal of rapidly rotating models is so strong that the entire waveform may be recovered for a galactic event.

For (2) and (3) we can attempt to give a heuristic answer on the basis of the mismatches computed between waveforms and the general simulation results: The short answer to both is likely "no." The long answer is slightly more involved: As we have demonstrated in Secs. V B and V C, both neutrino leakage and differences in progenitor structure/thermodynamics have an effect primarily on convective/turbulent dynamics driving GW emission in the region outside the PNS core that has stochastic character. So, despite the sizable mismatches listed in Tables III and IV, it will not be possible to make a case for telling $12-M_\odot/40-M_\odot$ or leakage/no-leakage models apart on the basis of the GW signal alone, since the shape (and perhaps even the overall characteristics) of the parts of the signal that differ are fundamentally unpredictable.

2. High-frequency variations in the neutrino luminosities

The dominant supernova neutrino reaction in water/ice-Cherenkov detectors is electron antineutrino capture on protons (e.g., [131]). We consider in our analysis the current detectors Super-Kamiokande [132] and IceCube [133], and the proposed future Hyper-Kamiokande detector [134]. A core-collapse event anywhere in the Milky Way is likely to be detected by these detectors with high SNR [132,133,135]. In the rapidly spinning protoneutron stars considered in this study, neutrino fluxes and average energies will generally be higher along the polar and lower along the equatorial direction as demonstrated by [25], who employed fully angle-dependent neutrino transport. The leakage scheme employed in this study does not allow us to make robust predictions of the flux asymmetry and we thus neglect it in the following discussion and leave its inclusion to future work.

Here we are interested in the question if the high-frequency variations in the rising neutrino luminosity seen in Fig. 3 are detectable. In consideration of the smallness of the effect, we pick a fiducial distance of 1 kpc for our estimates. More rigorous analyses of the detectability of time variations in the supernova neutrino signal, though for lower frequencies than considered here, were presented, e.g., by Burrows *et al.* [136], Lund *et al.* [27] and Brandt *et al.* [26]. For simplicity, we ignore neutrino oscillations in this analysis, but note that they may play an important role in the overall core-collapse supernova neutrino signature (e.g., [137]). Regarding the early postbounce signals considered here, one would expect some mixing of the $\bar{\nu}_e$ signal with the $\bar{\nu}_x$ signal [138]. However, since we observe similar rotation-induced variations in the ν_x signal (Fig. 3), we expect approximately the same results for a mixed $\bar{\nu}_e$ signal.

In Fig. 14, we plot the early $\bar{\nu}_e$ signal for model s12WH07j5 and superpose the error bars for the statistical error of the estimated recovered luminosity in Super-Kamiokande, Hyper-Kamiokande, and IceCube for a source distance of 1 kpc. The results are very similar for model s12WH07j4 and for the corresponding models using the s40WH07 progenitor.

For the electron antineutrino capture rate on protons in water-Cherenkov detectors we obtain an estimate based on [139,140],

$$R^{\rm SK/HK}_{\bar{\nu}_e} \sim \frac{L_{\bar{\nu}_e}}{4\pi r^2}\,\frac{\sigma_0(1+3g_A^2)}{4m_e^2c^4}\,\frac{\langle E^2_{\bar{\nu}_e}\rangle}{\langle E_{\bar{\nu}_e}\rangle}\,\frac{M_{\rm SK/HK}X_{\rm p}}{m_{\rm p}}, \qquad (23)$$

where $\sigma_0 = 1.76\times10^{-44}\ {\rm cm}^2$ is the reference weak-interaction cross section, $g_A = -1.254$ is the axial coupling constant, $M_{\rm SK} = 22.4$ kT, $M_{\rm HK} = 740$ kT is the

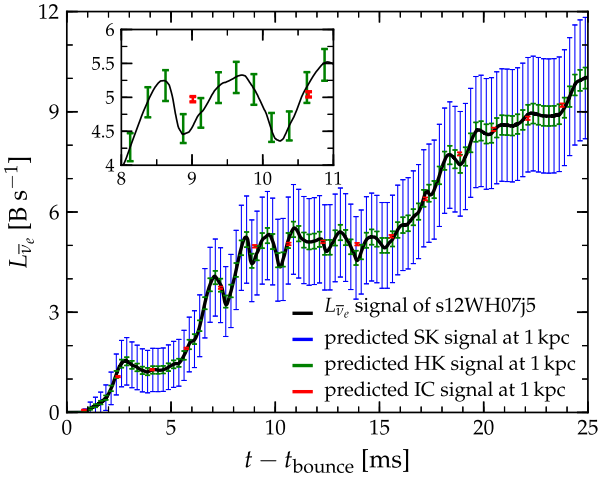

FIG. 14 (color online). Predicted neutrino signals and associated statistical error in Super-Kamiokande (SK, blue error bars), Hyper-Kamiokande (HK, green error bars), and IceCube (IC, red error bars) from model s12WH07j5 at 1 kpc. The solid black line is the $\bar{\nu}_e$ luminosity from our simulation. In the inset we show only the HK and IC predicted signals and errors, zoomed in between 8 and 11 ms. The error of the IC signal is small, but the imposed bin width of 1.6384 ms averages out variations on time scales smaller than this. If binned in 1.6384-ms bins, the Hyper-Kamiokande SNR would be approximately half of the SNR in IceCube.

fiducial water mass of Super-Kamiokande and Hyper-Kamiokande, respectively, $X_{\rm p}$ is the number fraction of protons (for H_2O, $X_{\rm p} = 2/18$), $m_{\rm p}$ is the proton mass, and $\langle E^2\rangle/\langle E\rangle$ is the energy-averaged spectral factor. We take $T_{\bar{\nu}_e} \sim 4$ MeV and zero chemical potential as an approximation, giving $\langle E^2\rangle/\langle E\rangle \sim 16.4$ MeV. With these numbers, for Super-Kamiokande, $R^{\rm SK}_{\bar{\nu}_e} \sim 12000\ {\rm s}^{-1} L_{\bar{\nu}_e,51}/r^2_{1\ {\rm kpc}}$ and for Hyper-Kamiokande, $R^{\rm HK}_{\bar{\nu}_e} \sim 400000\ {\rm s}^{-1} L_{\bar{\nu}_e,51}/r^2_{1\ {\rm kpc}}$, where $L_{\bar{\nu}_e,51}$ is the electron antineutrino luminosity in units of 10^{51} erg s^{-1} and $r_{1\ {\rm kpc}}$ is the distance in kiloparsecs.

In Super/Hyper-Kamiokande, electron antineutrino events are detected individually; therefore, if the signal is strong enough, one can bin the events in temporal bins of almost arbitrarily small width. To capture the rotation-induced variations, we choose bin widths of 0.25 ms. As seen in Fig. 14, within statistical errors, Super-Kamiokande is insensitive to the variations, even at 1 kpc for model s12WH07j5. Hyper-Kamiokande, however, has ~33 times the sensitivity of Super-Kamiokande and would be able to marginally detect our predicted oscillations if the collapsing core was rapidly rotating and within 1 kpc. Super-Kamiokande and Hyper-Kamiokande are sensitive to the total electron antineutrino signal at 25 ms with an estimated signal-to-noise ratio of 6 and 35, respectively, at this distance.

For IceCube we use the rate prediction of [138]. The expected event rate per 1.6384-ms timing sample in IceCube from electron antineutrino interactions in the ice is

$$R^{\rm IceCube}_{\bar{\nu}_e} = 1860\left(\frac{L_{\bar{\nu}_e}}{1{\rm B\ s}^{-1}}\right)\left(\frac{1\ {\rm kpc}}{r}\right)^2 \frac{\langle E^3_{15}\rangle}{\langle E_{15}\rangle}\ {\rm bin}^{-1} \qquad (24)$$

where, following [138], we assume $\langle E\rangle = 15$ MeV and take the spectral factor $\langle E^3\rangle/\langle E\rangle^3 \sim 2$; this gives $R^{\rm IC}_{\bar{\nu}_e} \sim 2.3 \times 10^6\ {\rm s}^{-1} L_{\bar{\nu}_e,51}/r^2_{1\ {\rm kpc}}$. We estimate the errors based on IceCube's background root-mean-square scatter of ~47 events bin^{-1} [138] and the square root of the expected count rate. IceCube is very sensitive to the overall $L_{\bar{\nu}_e}$ signal of model s12WH07j5 at a distance of 1 kpc ($L_{\bar{\nu}_e} = 9.20 \pm 0.05$ B s^{-1} at 24 ms after bounce). This is due to both the large effective volume that IceCube covers, ~3.5 Mt or $\sim 5 \times M_{\rm HK}$, and the current relatively large (compared to our choice for Super- and Hyper-Kamiokande) 1.6384 ms binning of the IceCube detector. Unfortunately, this large bin width makes it impossible to resolve the short-period (1.2–1.3 ms) variations in $L_{\bar{\nu}_e}$ in IceCube, even if one applied a subsampling method as proposed by [141]. We also note that at close distances ($\lesssim$ 1-few kpc), detector saturation due to the high event rate may prevent an accurate determination of the neutrino luminosity [133].

VI. SUMMARY AND CONCLUSIONS

We have presented results from a new set of (octant) 3D fully GR rotating core-collapse simulations. These simulations are the first to be carried out with a microphysical EOS, progenitor models from stellar evolution simulations, a parametrized treatment of deleptonization during collapse and deleptonization and neutrino cooling/heating in the postbounce phase via an approximate neutrino leakage scheme. Our simulations track collapse, bounce, and the first 25 ms of the postbounce phase. We considered pre-collapse rotation rates that lead to early postbounce PNS spin periods as short as ~1.5 ms. Such rapid rotation is not expected for garden-variety core-collapse supernovae (e.g., [15,16]), but may be highly relevant for potentially jet-driven explosions in the context of hyperenergetic core-collapse supernovae and long gamma-ray bursts. Our simulations are an extension of previous work by Dimmelmeier *et al.* [44], who performed a large suite of 2D conformally flat GR rotating core-collapse simulations with similar microphysics and progenitor models, but neglected postbounce neutrino leakage.

The major new result of this study is the discovery of a systematic correlation between high-frequency (~700–800 Hz) variations in the GW signal and in the luminosities of electron antineutrinos and heavy-lepton neutrinos. These are induced by nonlinear global oscillations of the PNS that are excited at core bounce in rapidly rotating cores. Detailed analysis of the nature of the rotationally induced PNS oscillation indicates that the excited mode is the fundamental quadrupole pulsation mode of the PNS. We find that an inner core ratio of rotational kinetic energy to gravitational energy ($T/|W|$) at bounce of $\gtrsim 5\%$ (corresponding to a PNS with spin period $\lesssim 2.5$ ms in our

models) is required for the oscillations to be excited at significant amplitudes. This requires an inner core angular momentum $\gtrsim 2 \times 10^{48}$ g cm^{-3} s^{-1} at an inner core mass of ~ 0.5–$0.7 M_\odot$ at bounce and is independent of other progenitor properties.

Thus, neutrinos and gravitational waves can both be used to probe rapid rotation in core collapse and combined can provide smoking-gun evidence for core rotation at the level required to drive magnetorotational explosions in the context of hyperenergetic core-collapse supernovae (e.g., [13,14]). However, while the GW signal is likely to be detectable throughout the Milky Way by the advanced generation of laser interferometer GW observatories, a water-Cherenkov detector would have to be of the scale of the planned Hyper-Kamiokande to observe the oscillations in the electron antineutrino luminosity at a source distance of only 1 kpc. IceCube, on the other hand, would in principle have the sensitivity to detect the oscillations at distances of $\sim$1–2 kpc, but lacks the necessary timing resolution.

Each model simulation carried out in this study was run once with and once without postbounce neutrino leakage. Comparing the two cases, we find that deleptonization and neutrino cooling/heating in the region behind the stalled shock have a strong effect on the radius of the stalled shock, on the convective dynamics in the region behind the shock, and on the associated GW signal. The GW signal from convective dynamics dominates the GW emission in nonrotating and slowly rotating cores, but its detailed shape is impossible to predict exactly, due to its inherently stochastic nature and its dependence on the unknown magnitude and location of seed perturbations and the detailed thermodynamics of the collapsed core. In moderately rapidly and rapidly rotating models (with $T/|W|$ at bounce $\gtrsim 1.5\%$), the GW emission is dominated by the dynamics of the inner core in which neutrinos are trapped and leak out only on a diffusion time scale. The overall GW signal of these models shows little sensitivity to postbounce neutrino leakage, which lends credence to the results of Dimmelmeier *et al.* [44], who neglected postbounce leakage.

Investigating the dependence of rotating collapse dynamics and GW signals on the progenitor star zero-age main-sequence mass, we performed simulations with a $12 - M_\odot$ and a $40 - M_\odot$ presupernova model drawn from [69]. For each progenitor model, we carried out six simulations, varying the precollapse rotation from zero to very rapid and setting up rotation in a way to ensure that both progenitors were endowed with nearly the same angular momentum as a function of enclosed mass.

The results of this progenitor comparison show that the GW signal of rapidly rotating core collapse and the early postbounce evolution is essentially independent of progenitor structure and thermodynamics and is determined primarily by the mass and angular momentum of the inner core at bounce. This finding is in contrast to previous work in which progenitor dependence was studied, but in which rotation was parametrized either by the precollapse central angular velocity $\Omega_{c,\mathrm{initial}}$ [44] or by choosing an initial value of $T/|W|$. Both $\Omega_{c,\mathrm{initial}}$ and initial $T/|W|$ are not directly observable in nature and both lead to inner core angular momentum that depends sensitively on how far the inner regions of the presupernova models have already collapsed when rotation is imposed at the time of mapping from the stellar evolution code into the collapse code. This introduces an essentially arbitrary factor in the rotational setup and makes it impossible to infer the true precollapse rotational configuration from GW (and neutrino) observations. In previous work, this systematic problem with $\Omega_{c,\mathrm{initial}}$ and initial $T/|W|$ as parameters for rotation was not fully realized, which has lead to misinterpretations of simulation results.

Two aspects of rotating core-collapse evolution not addressed in this study are the dependence of the dynamics and resulting GW signal on the nuclear EOS and on the degree of precollapse differential rotation. The dependence on the former has been studied to some extent by [44,47], who found quantitative, but not qualitative differences in the emitted GW signals that may be recovered by GW observations of a nearby event [32]. Since the frequency of the fundamental quadrupole pulsation mode depends on PNS structure, one would expect at least a slight variation with EOS of the early-postbounce GW and neutrino signal frequencies in rapidly spinning models. This is an interesting possibility that should be considered in future work. Strong differential rotation, though currently not deemed likely in precollapse iron cores, could potentially lead to significant qualitative differences that so far have been explored only with simpler approaches [28,37,38,41]. Furthermore, for application of simulated GW signals in advanced GW detector data analysis (e.g., [32,34]), extensive fine-grained parameter studies with probably hundreds of simulated models are necessary. The 12 new waveforms resulting from this study, which we make available at [142], are too few and too coarsely sample the parameter space to provide useful guides for GW data analysis.

The work presented in this paper marks a sizable, though incremental, step towards realistic 3D GR models of rotating core collapse and postbounce supernova evolution and reliable predictions of GW and neutrino signals. It complements the recent groundbreaking study of Kuroda *et al.* [143], who performed 3D GR simulations at modest resolution to $\sim$100 ms after bounce without symmetry constraints and with a single nonrotating progenitor, using similar microphysical detail and neutrino approximations.

Since our focus here has been on the collapse and early postbounce evolution during which 3D and MHD effects are likely small [13,47,57], the most severe limitation of our work is the reliance on parametrized deleptonization during collapse and on the energy-averaged neutrino

leakage scheme for deleptonization, cooling, and heating after bounce. While we expect the qualitative features and quantitative trends to be robust and hold when a more accurate neutrino treatment is employed, the technical limitations of our simulations must be taken into account when considering the results of this study. In particular, the newly identified correlation between GW signal and neutrino luminosities in rapidly rotating cores must receive further scrutiny, for example, by the 2D conformally flat GR approach of Müller *et al.* [3] that implements neutrino-transport in a ray-by-ray two-moment approach with a variable Eddington factor determined by a full solution of the Boltzmann equation. This approach would allow one to also extract the low-frequency GW signal due to anisotropic neutrino emission, which is likely to be of sizable amplitude due to the large rotationally induced flux anisotropy in rotating models (e.g., [25,28]), but could not be considered here due to the limitations of our leakage scheme.

Our future work in 3D GR will be directed towards extending our simulations to full 3D and including MHD to study 3D rotational instabilities and magnetic-field-driven dynamics. We will also explore improved treatments of neutrino transport that are computationally efficient and scale to full 3D simulations, e.g., the Monte Carlo approach to neutrino transport laid out by Abdikamalov *et al.* [144].

ACKNOWLEDGMENTS

We are happy to acknowledge helpful exchanges with Y. Chen, C. Cutler, L. Dessart, I. Hawke, W. Kastaun, F. Löffler, C. Meakin, P. Mösta, N. Stergioulas, P. Ajith, and D. Tsang. This work is supported by the National Science Foundation under Grants No. AST-0855535, No. OCI-0905046, and No. OCI-0941653, and by the Sherman Fairchild Foundation and the Alfred P. Sloan Foundation. We wish to thank Chris Mach for support of the group servers at TAPIR on which much of the code development and testing was carried out. Results presented in this article were obtained through computations on the Caltech compute cluster "Zwicky" (NSF MRI Grant No. PHY-0960291), on the NSF XSEDE network under Grant No. TG-PHY100033, on machines of the Louisiana Optical Network Initiative under Grant No. loni_numrel07, and at the National Energy Research Scientific Computing Center (NERSC), which is supported by the Office of Science of the U. S. Department of Energy under Contract No. DE-AC03-76SF00098.

[1] H.-T. Janka, K. Langanke, A. Marek, G. Martínez-Pinedo, and B. Müller, Phys. Rep. **442**, 38 (2007).
[2] E. O'Connor and C. D. Ott, Astrophys. J. **730**, 70 (2011).
[3] B. Müller, H.-T. Janka, and A. Marek, arXiv:1202.0815 [Astrophys. J. (to be published)].
[4] S. W. Bruenn, A. Mezzacappa, W. R. Hix, J. M. Blondin, P. Marronetti, O. E. B. Messer, C. J. Dirk, and S. Yoshida, in *Probing Stellar Populations Out to the Distant Universe*, edited by G. Giobbi, A. Tornambe, G. Raimondo, M. Limongi, L. A. Antonelli, N. Menci, and E. Brocato, AIP Conf. Proc. No. 1111 (AIP, New York, 2009).
[5] J. Nordhaus, A. Burrows, A. Almgren, and J. Bell, Astrophys. J. **720**, 694 (2010).
[6] T. Takiwaki, K. Kotake, and Y. Suwa, Astrophys. J. **749**, 98 (2012).
[7] I. Sagert, T. Fischer, M. Hempel, G. Pagliara, J. Schaffner-Bielich, A. Mezzacappa, F. Thielemann, and M. Liebendörfer, Phys. Rev. Lett. **102**, 081101 (2009).
[8] A. Burrows, E. Livne, L. Dessart, C. D. Ott, and J. Murphy, Astrophys. J. **640**, 878 (2006).
[9] S. A. Balbus and J. F. Hawley, Astrophys. J. **376**, 214 (1991).
[10] M. Obergaulinger, P. Cerdá-Durán, E. Müller, and M. A. Aloy, Astron. Astrophys. **498**, 241 (2009).
[11] G. S. Bisnovatyi-Kogan, Astron. Zh. **47**, 813 (1970).
[12] J. M. LeBlanc and J. R. Wilson, Astrophys. J. **161**, 541 (1970).
[13] A. Burrows, L. Dessart, E. Livne, C. D. Ott, and J. Murphy, Astrophys. J. **664**, 416 (2007).
[14] T. Takiwaki and K. Kotake, Astrophys. J. **743**, 30 (2011).
[15] C. D. Ott, A. Burrows, T. A. Thompson, E. Livne, and R. Walder, Astrophys. J. Suppl. Ser. **164**, 130 (2006).
[16] A. Heger, S. E. Woosley, and H. C. Spruit, Astrophys. J. **626**, 350 (2005).
[17] S. E. Woosley and A. Heger, Astrophys. J. **637**, 914 (2006).
[18] S.-C. Yoon, N. Langer, and C. Norman, Astron. Astrophys. **460**, 199 (2006).
[19] S. E. Woosley and J. S. Bloom, Annu. Rev. Astron. Astrophys. **44**, 507 (2006).
[20] A. M. Soderberg, S. Chakraborti, G. Pignata, R. A. Chevalier, P. Chandra, A. Ray, M. H. Wieringa, A. Copete, V. Chaplin, V. Connaughton *et al.*, Nature (London) **463**, 513 (2010).
[21] D. Kasen and L. Bildsten, Astrophys. J. **717**, 245 (2010).
[22] S. E. Woosley, Astrophys. J. Lett. **719**, L204 (2010).
[23] A. L. Piro and C. D. Ott, Astrophys. J. **736**, 108 (2011).
[24] A. Marek, H.-T. Janka, and E. Müller, Astron. Astrophys. **496**, 475 (2009).
[25] C. D. Ott, A. Burrows, L. Dessart, and E. Livne, Astrophys. J. **685**, 1069 (2008).
[26] T. D. Brandt, A. Burrows, C. D. Ott, and E. Livne, Astrophys. J. **728**, 8 (2011).
[27] T. Lund, A. Marek, C. Lunardini, H.-T. Janka, and G. Raffelt, Phys. Rev. D **82**, 063007 (2010).
[28] C. D. Ott, Classical Quantum Gravity **26**, 063001 (2009).
[29] K. N. Yakunin, P. Marronetti, A. Mezzacappa, S. W. Bruenn, C.-T. Lee, M. A. Chertkow, W. R. Hix,

J. M. Blondin, E. J. Lentz, O. E. Bronson Messer *et al.*, Classical Quantum Gravity **27**, 194005 (2010).
[30] J. W. Murphy, C. D. Ott, and A. Burrows, Astrophys. J. **707**, 1173 (2009).
[31] K. Kotake, arXiv:1110.5107 [C.R. Physique (to be published)].
[32] C. Röver, M. Bizouard, N. Christensen, H. Dimmelmeier, I. S. Heng, and R. Meyer, Phys. Rev. D **80**, 102004 (2009).
[33] C. D. Ott, Classical Quantum Gravity **26**, 204015 (2009).
[34] J. Logue, C. D. Ott, I. S. Heng, P. Kalmus, and J. Scargill, arXiv:1202.3256 [Phys. Rev. D (to be published)].
[35] E. Müller, Astron. Astrophys. **114**, 53 (1982).
[36] R. Mönchmeyer, G. Schäfer, E. Müller, and R. Kates, Astron. Astrophys. **246**, 417 (1991).
[37] K. Kotake, S. Yamada, and K. Sato, Phys. Rev. D **68**, 044023 (2003).
[38] C. D. Ott, A. Burrows, E. Livne, and R. Walder, Astrophys. J. **600**, 834 (2004).
[39] T. Zwerger and E. Müller, Astron. Astrophys. **320**, 209 (1997).
[40] S. Yamada and K. Sato, Astrophys. J. **450**, 245 (1995).
[41] H. Dimmelmeier, J. A. Font, and E. Müller, Astron. Astrophys. **393**, 523 (2002).
[42] M. Shibata and Y. Sekiguchi, Phys. Rev. D **69**, 084024 (2004).
[43] H. Dimmelmeier, C. D. Ott, H.-T. Janka, A. Marek, and E. Müller, Phys. Rev. Lett. **98**, 251101 (2007).
[44] H. Dimmelmeier, C. D. Ott, A. Marek, and H.-T. Janka, Phys. Rev. D **78**, 064056 (2008).
[45] P. Cerdá-Durán, J. A. Font, L. Antón, and E. Müller, Astron. Astrophys. **492**, 937 (2008).
[46] E. B. Abdikamalov, C. D. Ott, L. Rezzolla, L. Dessart, H. Dimmelmeier, A. Marek, and H. Janka, Phys. Rev. D **81**, 044012 (2010).
[47] S. Scheidegger, R. Käppeli, S. C. Whitehouse, T. Fischer, and M. Liebendörfer, Astron. Astrophys. **514**, A51 (2010).
[48] K. Kotake, S. Yamada, K. Sato, K. Sumiyoshi, H. Ono, and H. Suzuki, Phys. Rev. D **69**, 124004 (2004).
[49] M. Obergaulinger, M. A. Aloy, and E. Müller, Astron. Astrophys. **450**, 1107 (2006).
[50] M. Obergaulinger, M. A. Aloy, H. Dimmelmeier, and E. Müller, Astron. Astrophys. **457**, 209 (2006).
[51] M. Shibata, Y. T. Liu, S. L. Shapiro, and B. C. Stephens, Phys. Rev. D **74**, 104026 (2006).
[52] S. Scheidegger, T. Fischer, S. C. Whitehouse, and M. Liebendörfer, Astron. Astrophys. **490**, 231 (2008).
[53] S. Bonazzola and J. A. Marck, Astron. Astrophys. **267**, 623 (1993).
[54] M. Rampp, E. Müller, and M. Ruffert, Astron. Astrophys. **332**, 969 (1998).
[55] M. Shibata and Y.-I. Sekiguchi, Phys. Rev. D **71**, 024014 (2005).
[56] N. Andersson, Classical Quantum Gravity **20**, R105 (2003).
[57] C. D. Ott, H. Dimmelmeier, A. Marek, H.-T. Janka, I. Hawke, B. Zink, and E. Schnetter, Phys. Rev. Lett. **98**, 261101 (2007).
[58] C. D. Ott, H. Dimmelmeier, A. Marek, H.-T. Janka, B. Zink, I. Hawke, and E. Schnetter, Classical Quantum Gravity **24**, S139 (2007).
[59] A. L. Watts, N. Andersson, and D. I. Jones, Astrophys. J. Lett. **618**, L37 (2005).
[60] W. Fu and D. Lai, Mon. Not. R. Astron. Soc. **413**, 2207 (2011).
[61] R. Walder, A. Burrows, C. D. Ott, E. Livne, I. Lichtenstadt, and M. Jarrah, Astrophys. J. **626**, 317 (2005).
[62] T. A. Thompson, E. Quataert, and A. Burrows, Astrophys. J. **620**, 861 (2005).
[63] F. Löffler, J. Faber, E. Bentivegna, T. Bode, P. Diener, R. Haas, I. Hinder, B. C. Mundim, C. D. Ott, E. Schnetter *et al.*, Classical Quantum Gravity **29**, 115001 (2012).
[64] Einstein Toolkit: A Community Toolkit for Numerical Relativity, http://www.einsteintoolkit.org.
[65] J. M. Lattimer and F. D. Swesty, Nucl. Phys. **A535**, 331 (1991).
[66] C. D. Ott, E. P. O'Connor, and B. Dasgupta, arXiv:1111.6282.
[67] A. W. Steiner, J. M. Lattimer, and E. F. Brown, Astrophys. J. **722**, 33 (2010).
[68] K. Hebeler, J. M. Lattimer, C. J. Pethick, and A. Schwenk, Phys. Rev. Lett. **105**, 161102 (2010).
[69] S. E. Woosley and A. Heger, Phys. Rep. **442**, 269 (2007).
[70] T. Goodale, G. Allen, G. Lanfermann, J. Massó, T. Radke, E. Seidel, and J. Shalf, in *Vector and Parallel Processing, VECPAR'2002, 5th International Conference, Lecture Notes in Computer Science* (Springer, Berlin, 2003).
[71] Cactus Computational Toolkit home page, http://www.cactuscode.org/.
[72] T. W. Baumgarte and S. L. Shapiro, Phys. Rev. D **59**, 024007 (1998).
[73] M. Shibata and T. Nakamura, Phys. Rev. D **52**, 5428 (1995).
[74] M. Alcubierre, B. Brügmann, T. Dramlitsch, J. A. Font, P. Papadopoulos, E. Seidel, N. Stergioulas, and R. Takahashi, Phys. Rev. D **62**, 044034 (2000).
[75] M. Alcubierre, B. Brügmann, P. Diener, M. Koppitz, D. Pollney, E. Seidel, and R. Takahashi, Phys. Rev. D **67**, 084023 (2003).
[76] D. Brown, P. Diener, O. Sarbach, E. Schnetter, and M. Tiglio, Phys. Rev. D **79**, 044023 (2009).
[77] C. Reisswig, C. D. Ott, U. Sperhake, and E. Schnetter, Phys. Rev. D **83**, 064008 (2011).
[78] J. A. Font, Living Rev. Relativity **11**, 7 (2008).
[79] B. Einfeldt, in *Shock Tubes and Waves, Proceedings of the Sixteenth International Symposium, Aachen, Germany, 26–31, 1987* (VCH Verlag, Weinheim, Germany, 1988), p. 671.
[80] P. Colella and P. R. Woodward, J. Comput. Phys. **54**, 174 (1984).
[81] J. M. Hyman, *Tech. Report, ERDA Mathematics and Computing Laboratory, Courant Institute of Mathematical Sciences* (New York University, New York, 1976).
[82] E. Schnetter, S. H. Hawley, and I. Hawke, Classical Quantum Gravity **21**, 1465 (2004).
[83] M. J. Berger and J. Oliger, J. Comput. Phys. **53**, 484 (1984).
[84] P. B. Demorest, T. Pennucci, S. M. Ransom, M. S. E. Roberts, and J. W. T. Hessels, Nature (London) **467**, 1081 (2010).
[85] E. O'Connor and C. D. Ott, Classical Quantum Gravity **27**, 114103 (2010).
[86] E. O'Connor and C. D. Ott, Proc. Sci., NIC XI (2010) 154.

[87] stellarcollapse.org: A Community Portal for Stellar Collapse, Core-Collapse Supernova and GRB Simulations, http://www.stellarcollapse.org.

[88] M. Liebendörfer, Astrophys. J. **633**, 1042 (2005).

[89] R. Buras, M. Rampp, H.-T. Janka, and K. Kifonidis, Astron. Astrophys. **447**, 1049 (2006).

[90] C. D. Ott *et al.*, Supplemental Data for Correlated Gravitational Wave and Neutrino Signals from General-Relativistic Rapidly Rotating Iron Core Collapse, http://www.stellarcollapse.org/ccleakdata.

[91] S. Rosswog and M. Liebendörfer, Mon. Not. R. Astron. Soc. **342**, 673 (2003).

[92] M. Ruffert, H.-T. Janka, and G. Schäfer, Astron. Astrophys. **311**, 532 (1996).

[93] A. Burrows, J. Hayes, and B. A. Fryxell, Astrophys. J. **450**, 830 (1995).

[94] Y. Sekiguchi and M. Shibata, Astrophys. J. **737**, 6 (2011).

[95] C. Reisswig, N. T. Bishop, D. Pollney, and B. Szilagyi, Classical Quantum Gravity **27**, 075014 (2010).

[96] C. D. Ott, C. Reisswig, E. Schnetter, E. O'Connor, U. Sperhake, F. Löffler, P. Diener, E. Abdikamalov, I. Hawke, and A. Burrows, Phys. Rev. Lett. **106**, 161103 (2011).

[97] B. F. Schutz, *A First Course in General Relativity* (Cambridge University Press, Cambridge, England, 1985).

[98] L. S. Finn and C. R. Evans, Astrophys. J. **351**, 588 (1990).

[99] L. Blanchet, T. Damour, and G. Schaefer, Mon. Not. R. Astron. Soc. **242**, 289 (1990).

[100] H. Dimmelmeier, J. A. Font, and E. Müller, Astron. Astrophys. **388**, 917 (2002).

[101] K. S. Thorne, Rev. Mod. Phys. **52**, 299 (1980).

[102] É. É. Flanagan and S. A. Hughes, Phys. Rev. D **57**, 4535 (1998).

[103] D. Shoemaker (LIGO Scientific Collaboration), Tech. Report No. LIGO-T0900288-v3 [https://dcc.ligo.org/cgi-bin/DocDB/ShowDocument?docid=t0900288] 2010.

[104] B. J. Owen, Phys. Rev. D **53**, 6749 (1996).

[105] T. Damour, B. R. Iyer, and B. S. Sathyaprakash, Phys. Rev. D **57**, 885 (1998).

[106] C. Reisswig and D. Pollney, Classical Quantum Gravity **28**, 195015 (2011).

[107] L. Dessart, E. O'Connor, and C. D. Ott, arXiv:1203.1926 [Astrophys. J. (to be published)].

[108] A. Heger, N. Langer, and S. E. Woosley, Astrophys. J. **528**, 368 (2000).

[109] J.-L. Tassoul, *Theory of Rotating Stars* (Princeton University, Princeton, NJ, 1978).

[110] W. Kastaun, Ph. D. thesis, Eberhard Karls Universität Tübingen, Tübingen, Germany, 2007 [http://tobias-lib.uni-tuebingen.de/volltexte/2007/2803/].

[111] W. Unno, Y. Osaki, H. Ando, H. Saio, and H. Shibahashi, *Nonradial Oscillations of Stars* (University of Tokyo, Tokyo, 1989), 2nd ed..

[112] J. A. Font, H. Dimmelmeier, A. Gupta, and N. Stergioulas, Mon. Not. R. Astron. Soc. **325**, 1463 (2001).

[113] H. Dimmelmeier, N. Stergioulas, and J. A. Font, Mon. Not. R. Astron. Soc. **368**, 1609 (2006).

[114] A. Burrows and J. M. Lattimer, Astrophys. J. **270**, 735 (1983).

[115] K. Kotake, W. Iwakami, N. Ohnishi, and S. Yamada, Astrophys. J. Lett. **697**, L133 (2009).

[116] S. Chandrasekhar, *Ellipsoidal Figures of Equilibrium* (Yale University, New Haven, CT, 1987), revised ed..

[117] J. L. Friedman and B. F. Schutz, Astrophys. J. **222**, 281 (1978).

[118] S. Chandrasekhar, Astrophys. J. **161**, 561 (1970).

[119] D. Lai, in *Astrophysical Sources for Ground-Based Gravitational Wave Detectors,*, edited by J. M. Centrella, AIP Conf. Proc. No. 575 (AIP, New York, 2001).

[120] E. Gaertig and K. D. Kokkotas, Phys. Rev. D **83**, 064031 (2011).

[121] O. Korobkin, E. B. Abdikamalov, E. Schnetter, N. Stergioulas, and B. Zink, Phys. Rev. D **83**, 043007 (2011).

[122] J. M. Centrella, K. C. B. New, L. L. Lowe, and J. D. Brown, Astrophys. J. Lett. **550**, L193 (2001).

[123] M. Shibata, S. Karino, and Y. Eriguchi, Mon. Not. R. Astron. Soc. **343**, 619 (2003).

[124] S. Ou and J. E. Tohline, Astrophys. J. **651**, 1068 (2006).

[125] G. Corvino, L. Rezzolla, S. Bernuzzi, R. De Pietri, and B. Giacomazzo, Classical Quantum Gravity **27**, 114104 (2010).

[126] K. Kuroda (LCGT Collaboration), Classical Quantum Gravity **27**, 084004 (2010).

[127] G. Losurdo and D. Shoemaker (Virgo Collaboration), Tech. Report No. VIR-0174A-10 and LIGO-G1000176-v7, 2010.

[128] L. Wen and Y. Chen, Phys. Rev. D **81**, 082001 (2010).

[129] B. P. Abbott *et al.* (LIGO Scientific Collaboration), Rep. Prog. Phys. **72**, 076901 (2009).

[130] J. Abadie *et al.* (LIGO and Virgo Scientific Collaborations), Classical Quantum Gravity **27**, 173001 (2010).

[131] K. Scholberg, arXiv:1205.6003 [Annu. Rev. Nucl. Part. Sci. (to be published)].

[132] M. Ikeda *et al.* (Super-Kamiokande Collaboration), Astrophys. J. **669**, 519 (2007).

[133] R. Abbasi *et al.* (IceCube Collaboration), Astron. Astrophys. **535**, A109 (2011).

[134] K. Abe, T. Abe, H. Aihara, Y. Fukuda, Y. Hayato, K. Huang, A. K. Ichikawa, M. Ikeda, K. Inoue, H. Ishino *et al.*, arXiv:1109.3262.

[135] K. Scholberg, J. Phys. Conf. Ser. **309**, 012028 (2011).

[136] A. Burrows, D. Klein, and R. Gandhi, Phys. Rev. D **45**, 3361 (1992).

[137] H. Duan, G. M. Fuller, and Y.-Z. Qian, Annu. Rev. Nucl. Part. Sci. **60**, 569 (2010).

[138] F. Halzen and G. G. Raffelt, Phys. Rev. D **80**, 087301 (2009).

[139] P. Vogel and J. F. Beacom, Phys. Rev. D **60**, 053003 (1999).

[140] S. Horiuchi, J. F. Beacom, and E. Dwek, Phys. Rev. D **79**, 083013 (2009).

[141] B. Dasgupta, T. Fischer, S. Horiuchi, M. Liebendörfer, A. Mirizzi, I. Sagert, and J. Schaffner-Bielich, Phys. Rev. D **81**, 103005 (2010).

[142] C. D. Ott *et al.*, Gravitational Wave Catalog, http://www.stellarcollapse.org/gwcatalog.

[143] T. Kuroda, K. Kotake, and T. Takiwaki, arXiv:1202.2487 [Astrophys. J. (to be published)].

[144] E. Abdikamalov, A. Burrows, C. D. Ott, F. Löffler, E. O'Connor, J. C. Dolence, and E. Schnetter, arXiv:1203.2915 [Astrophys. J. (to be published)].

[145] S. E. Woosley, A. Heger, and T. A. Weaver, Rev. Mod. Phys. **74**, 1015 (2002).